Cool stellar wind modelling with PHOENIX

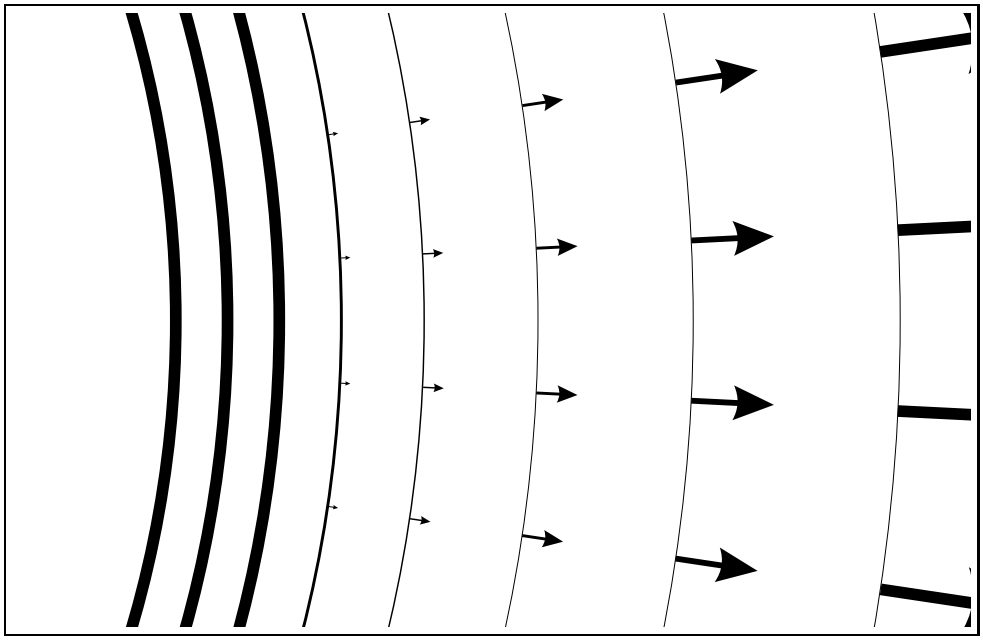

Diploma thesis
by
D.R. van Rossum

University of Hamburg
May 31, 2006

Zusammenfassung

Es gibt derzeit noch keine vollstaendige, selbst-konsistente, theoretische Beschreibung von kuehlen Winden, die ihre beobachteten grundlegenden Eigenschaften beschreiben kann. Um weitere Fortschritte bei der Suche nach einer theoretischen Beschreibung zu ermoeglichen, sind detaillierte Kenntnisse der Struktur von Atmosphaeren kuehler Winde erforderlich.

In dieser Arbeit ist das "hot-wind" Modul von `PHOENIX`, ein hochentwickelter universeller Sternatmosphaerencode, modifiziert worden um damit kuehle Winde modellieren zu koennen.

Im modifizierten Code wird das radiale Gitter, das fuer den hydrodynamischen Teil der Atmosphaere benutzt wird, dynamisch angepasst. Damit wird erreicht, dass der Druck auf einen Bereich beschraenkt wird, der durch die Drucktabellen von `PHOENIX` unterstuetzt wird. Diese Tabellen werden werden fuer kuehle Atmosphaeren benoetigt. Hiermit wird auch fuer Winde mit niedriger Massenverlustrate an deren Fuss eine Bedingung erfuellt, durch die das optische-Tiefen-Gitter, dass fuer den hydrostatischen Teil der Atmosphaere generiert wird, brauchbare Schrittweiten bekommt. Ausserdem wird jetzt in der Atmosphaeren-Konstruktionsphase der Anfangszustand wiederhergestellt, wenn eine Iteration mit einem ungeeigneten Gitter ausgefuehrt wurde. So koennen weitere Iterationen mit einer unverdorbenen Struktur weiterrechnen.

Mit dem modifizierten Code koennen kuehle Winde gerechnet werden, fuer Parameterbereiche die mindestens $3200 < T_{\rm eff} < 4400$ K, $10^{-12} < \dot{M} < 10^{-6}$ $M_\odot$/yr and $10 < v_\infty < 120$ km/s umfassen, ohne dass eine Feinbestimmung weiterer Parameter notwendig waere.

Die synthetischen Spektren, die man mit `PHOENIX` berechnet, zeigen die charakteristischen beobachtete Eigenschaften von kuehlen Winden.

Es wird gezeigt, dass sich die obigen Parameterbereiche und die Genauigkeit der Modelrechnungen mit zwei Methoden verbessern lassen: eine verfeinerte Temperaturkorrektur-Methode und ein adaptiertes radiales Gitter.

Mit der Implementation dieser zusaetzlichen Verbesserungen und den vollstaendig "metal line-blanketing" NLTE Berechnungen bietet `PHOENIX` die Moeglichkeit sehr genaue Modelle fuer kuehle Winde zu berechnen.

Abstract

For cool winds no complete self-consistent theoretical description has yet been established which is able to reproduce the most basic observational findings. Further progress in finding a theoretical description of the driving mechanism requires a detailed knowledge of the structure of cool-wind atmospheres.

In this work the hot-wind module of PHOENIX, an advanced general-purpose stellar atmosphere code, has been modified to allow for cool-wind modelling.

In the modified code the radial grid used for the hydrodynamical part of the atmosphere is dynamically adjusted. This way a pressure range is obtained that can be handled with PHOENIX's pressure tables that are needed for cool atmospheres. In addition, winds with low mass loss rates at their bottom now provide a basis on which the optical depth grid, generated for the hydrostatic region, has feasible step widths. Furthermore, during the atmospheric construction the initial structure is restored after an iteration with an unsuitable grid. This provides subsequent iterations with an unmarred structure.

With the modified model, cool-winds can be computed without fine tuning for parameter ranges of at least $3200 < T_{\rm eff} < 4400$ K, $10^{-12} < \dot{M} < 10^{-6}$ $M_\odot$/yr and $10 < v_\infty < 120$ km/s.

The synthetic spectra obtained with PHOENIX show the characteristic observational features of cool-wind spectra.

It is shown that two methods will further improve the above parameter ranges and the accuracy of the model: a more sophisticated temperature correction method and an adapted radial grid.

With the implementation of these additional improvements, together with the support for full metal-line-blanketing NLTE computations, PHOENIX will give the opportunity to obtain most accurate cool-wind models.

Contents

1 Introduction

A stellar wind is a continuous outflow of material from a star. All stars are found to loose mass during a major fraction of their lives. The solar wind is a well-known phenomenon indirectly causing the northern light[1]. The solar wind was not observationally confirmed until 1962 by the Mariner 2 interplanetary probe. The crucial evidence for the existence of cool stellar winds, which this work is about, was found by Deutsch 1956 [Deu56]. A reason the cool type stellar wind could be found earlier than the solar wind is that the mass loss rate for cool winds is typically a factor of 10^7 larger than for the solar type winds. The large amounts of mass the star looses through this strong wind (up to half of the initial stellar mass) plays a major role for the evolution of the star.

But the origin of the cool winds has not yet been established since 1956. In order to find a theoretical self-consistent description a detailed knowledge of the structure of the wind is required. This must be achieved by perfecting the analysis of the observational spectra. The "reverse engineering" of cool-wind spectra is very intricate and model atmosphere calculations are used to find estimations for the structures of cool winds.

`PHOENIX` is a highly sophisticated general-purpose stellar atmosphere code that is capable of calculating expanding atmospheres. It has been used for hot-wind[2]model calculations, but not previously for cool winds. High precision cool wind modelling with `PHOENIX` could yield very tight parameter ranges to narrow down the "ansatz" for the theoretical description of the cool-wind driving mechanism. During the course of this work the `PHOENIX` wind model has been modified in order to allow for cool-wind calculations. With the modified code the cool-wind models are found to reproduce the critical observational characteristics of cool-wind spectra.

In the following chapter a general theoretical description of winds is given as well as the main properties of stellar winds and especially cool winds. In chapter 3 the way the wind model atmospheres are constructed is explained. This chapter also shows how `PHOENIX` calculates radiative transfer and how the constructed atmosphere is refined iteratively. The modifications made to the original wind model are described in chapter 4. Chapter 5 shows the results of cool-wind model calculations with the modified model. In chapter 6 these results are discussed and solutions for the remaining limitations are proposed as well as some concepts for further research in cool wind modelling with `PHOENIX` .

[1]The aurora is believed to be produced by an electric current that is driven by a "dynamo effect" between the solar wind and the earth's magnetosphere (two electric conductors at relative motion). It is not produced by solar wind particles guided by the Earth's field lines to the top of the atmosphere [Wik06].

[2]Hot winds are yet another class of stellar winds, different from cool-winds and solar type winds. The characteristics of the different classes are discussed in the next Chapter.

2 Stellar wind basics

Almost all stars are losing mass in the form of stellar winds through a major fraction of their lives. But the mechanisms that drive the winds vary for different classes of stars. A number of mechanisms have been proposed to drive gas out of the gravitational potential well of the star. Therefore, at first a physical description for an idealised simple wind will be set up. Then, the nature of the winds will be compared to the theoretical model, in order to draw some conclusions about the driving mechanisms involved. Thereafter, the observational methods to detect winds are described including the fundamental difficulties. Finally, a collection of empirical velocity fields found in the literature is examined in order to find a basis for the modelling process presented in chapter 3.

2.1 General theoretical description

For a time-independent stellar wind with constant mass loss rate, the amount of material passing through any sphere of radius r is constant

$$\dot{M}(r) = 4\pi r^2 \rho(r) v(r) = \dot{M} \tag{1}$$

Since the wind is stationary $\partial v(r,t)/\partial t = 0$, the wind velocity $v(r,t) = v(r)$ is a function of r only. The total derivative of $v(r,t)$ can be written as

$$\frac{\mathrm{d}v(r,t)}{\mathrm{d}t} = \frac{\partial v(r,t)}{\partial t} + \frac{\partial v(r,t)}{\partial r}\frac{\mathrm{d}r(t)}{\mathrm{d}t} = v(r)\frac{\mathrm{d}v}{\mathrm{d}r} \tag{2}$$

Suppose the gas of the wind is subjected to the inward directed gravity and the outward directed gas pressure force and an arbitrary force f per unit of mass. The equation of motion is then

$$v\frac{\mathrm{d}v}{\mathrm{d}r} + \frac{1}{\rho}\frac{\mathrm{d}p}{\mathrm{d}r} + \frac{GM_*}{r^2} = f \tag{3}$$

The first term on the left is the acceleration of the gas, which is produced by the gas pressure (second term), the gravity (third term) and the arbitrary force f. When the gas is assumed to behave like an ideal gas, the gas pressure is

$$p = \mathscr{R}\rho T/\mu \tag{4}$$

where $\mathscr{R}$ is the gas constant, ρ the density and μ the mean molecular weight expressed in units of m_H, which here is assumed to be constant throughout the wind. The isothermal speed of sound is given by

$$v_t^2 \equiv p/\rho = \mathscr{R}T/\mu \tag{5}$$

The force due to the pressure gradient can be written as

$$\frac{1}{\rho}\frac{\mathrm{d}p}{\mathrm{d}r} = \frac{v_t^2}{\rho}\frac{\mathrm{d}\rho}{\mathrm{d}r} + \frac{\mathrm{d}v_t^2}{\mathrm{d}r} = -v_t^2\frac{\mathrm{d}\ln v}{\mathrm{d}r} + \frac{\mathrm{d}v_t^2}{\mathrm{d}r} - \frac{2v_t^2}{r} \tag{6}$$

In the last step $\mathrm{d}\ln\rho = -\mathrm{d}\ln v - 2\mathrm{d}\ln r$ is used, which follows from the continuity equation (1). Substituting equation (6) into (3) yields

$$\frac{1}{v}\frac{\mathrm{d}v}{\mathrm{d}r} = \left(\frac{2v_t^2}{r} - \frac{\mathrm{d}v_t^2}{\mathrm{d}r} - \frac{GM_*}{r^2} + f\right)\left(v^2 - v_t^2\right)^{-1} \tag{7}$$

This equation is called the *momentum equation*. It describes the motion of the gas in a steady (time independent), radial, spherical symmetric stellar wind. The next step is to further idealise the model to extract the most basic properties of stellar winds.

2.1.1 Isothermal wind without additional forces

Let us first consider the most simple case of an isothermal wind $T(r) = T$ without extra forces $f = 0$. The first term on the right of Eq. (6) vanishes. Equation (7) then becomes

$$\frac{1}{v}\frac{\mathrm{d}v}{\mathrm{d}r} = \left(\frac{2v_t^2}{r} - \frac{v_g^2}{2r}\right)\left(v^2 - v_t^2\right)^{-1} \tag{8}$$

where the third term in the numerator on the right of Eq. (7) is rewritten using the gravitational escape velocity

$$v_g^2 \equiv \frac{2GM_*}{r} \tag{9}$$

This momentum equation has a singularity at the point r_s where $v(r_s) = v_t$, this is called the *sonic point*. There is another special point in the momentum equation that is called the *critical point*. At this point we have

$$v_t = v_g(r_c)/2 \tag{10}$$

and the numerator of Eq. (8) equals zero. $r_c = GM_*/2v_t^2$ is the critical distance. In this case of an isothermal wind without extra forces there is only a solution to the momentum equation if the sonic point coincides with the critical point.

The solutions of this momentum equation are plotted in figure 1. Curve 1 is the critical solution. It is transonic: it starts subsonic and ends supersonic. Curve 2 also passes through the critical point, but does not fulfill the boundary condition that the wind velocity should approach zero for small values of r. Curve 3 remains subsonic everywhere. This is not the kind of wind we try to describe, as observations show winds with a supersonic

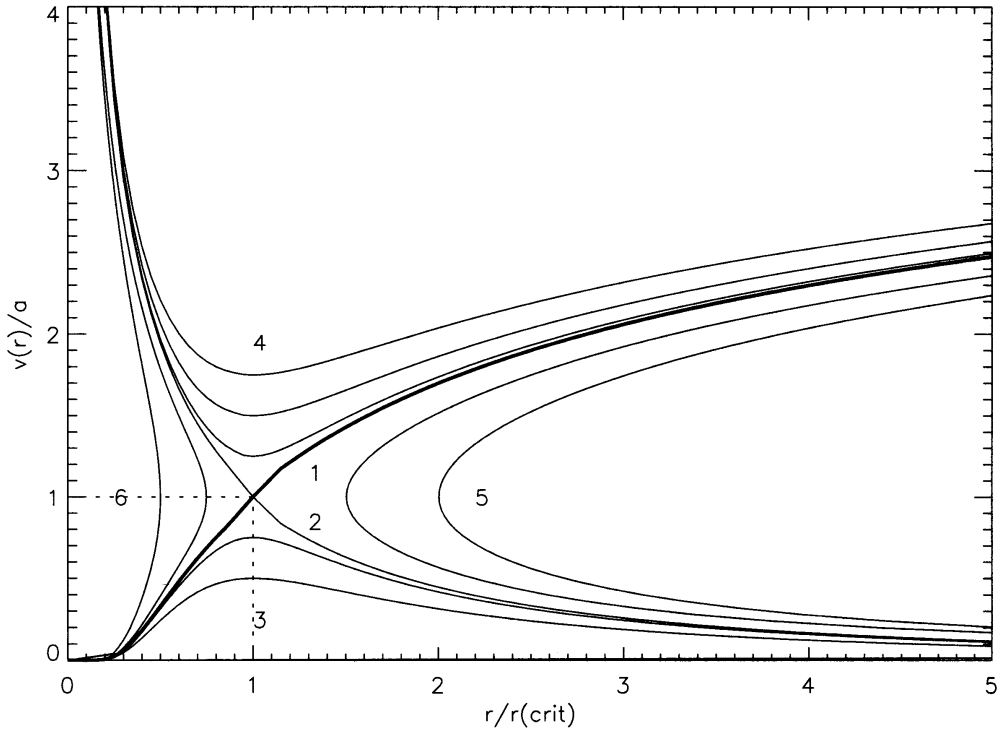

Figure 1: Solutions of the momentum equation for isothermal simple winds. It shows the velocity structure of an isothermal wind with gas pressure and gravity forces only. The radius is in units of critical radius, r_c, the velocity in units of the isothermal speed of sound, v_t, here denoted by a. Curve 1 is the unique transonic solution with increasing velocity through the critical point where the wind velocity equals the isothermal speed of sound. (from [LC99])

terminal velocity (see page 11-13 for the properties of such winds). Curve 4 again has an unphysical supersonic starting velocity. Curve 5 and 6 are mathematical solutions which do not have a physical meaning.

Solving equation (8) analytically [Par58] and using the condition for the critical point $v(r_c) = v_t$ yields

$$\frac{v}{v_t} = \left(\frac{r_c}{r}\right)^2 \exp\left(-\frac{2r_c}{r} + \frac{3}{2} + \frac{v^2}{2v_t^2}\right) \tag{11}$$

The initial velocity v_0 at the base of a gravitationally bound wind r_0 with $v_0^2 \ll v_t^2$ can now be expressed as

$$\frac{v_0}{v_t} = \left(\frac{v_{g0}^2}{4v_t^2}\right)^2 \exp\left(-\frac{v_{g0}^2}{2v_t^2} + \frac{3}{2}\right) \tag{12}$$

where $v_{g0} = v_g(r_0)$ is the gravitational escape velocity at the base of the

wind. The mass loss rate is determined by this base velocity through the mass continuity equation $\dot{M} = 4\pi f \propto v_0$. If the stellar atmosphere is strongly gravitationally bound at its base, $v_{g0}^2 \gg 2v_t^2$, then the mass loss rate is dominated by the exponential term of Eq. (12). So an increasing atmospheric temperature leads to strong increase of $\dot{M}$. If the atmosphere is not strongly gravitationally bound $v_{g0}^2 \gtrsim 2v_t^2$ holds. The second term in the exponent of Eq. (12) exceeds the first, so that influence of the quadratic factor increases. And since the quadratic dependency is much weaker than the exponential the dependence of the mass flux on the atmospheric temperature then is much weaker

2.1.2 Adiabatic wind

The model restrictions of the previous paragraph are eased to obtain a more general model: the temperature is variable and forces additional to the gravity and the pressure gradient force are accounted for. A useful way to set up this model is to use the energy per unit mass, $e(r)$, which is the sum of the kinetic and gravitational energies, and the enthalpy [LC99].

$$e(r) = \frac{v(r)^2}{2} - \frac{GM_*}{r} + \frac{\gamma}{\gamma - 1}\frac{\mathscr{R}T}{\mu} \tag{13}$$

In this expression γ is the ratio of specific heats $\gamma = c_p/c_v$. The enthalpy is the sum of the internal energy of the gas and the potential for work by adiabatic expansion. For an ideal gas, these are $2/3\mathscr{R}T/\mu$ and $\mathscr{R}T/\mu$ respectively, yielding a value of $\gamma = 5/3$. Energy can be added to the wind if form of work done by a force or in the form of heat:

$$\frac{\mathrm{d}}{\mathrm{d}r}\left(\frac{v^2}{2} - \frac{GM_*}{r} + v_t^2\frac{\gamma}{\gamma - 1}\right) = \frac{\mathrm{d}e(r)}{\mathrm{d}r} = f + q \tag{14}$$

with f the force per unit of mass and q the gradient of the heat addition per unit mass. This can be rewritten to

$$\frac{\mathrm{d}v_t^2}{\mathrm{d}r} = \frac{\gamma - 1}{\gamma}\left(f + q - \frac{GM_*}{r^2} - v\frac{\mathrm{d}v}{\mathrm{d}r}\right) \tag{15}$$

Insterting (15) into the momentum equation (7) and using $2GM_*/r = v_g^2$ one obtains after multiplying the result with γ

$$\frac{1}{v}\frac{\mathrm{d}v}{\mathrm{d}r} = \left(\frac{2v_s^2}{r} - \frac{v_g^2}{2r} + f - (\gamma - 1)q\right)\left(v^2 - v_s^2\right)^{-1} \tag{16}$$

Here $v_s = \sqrt{\gamma v_t^2}$ is the adiabatic speed of sound. There are three differences between this adiabatic momentum equation (16) and the isothermal momentum equation (8). Firstly, $f \neq 0$. Secondly, the isothermal speed of

sound v_t is replaced with the adiabatic version v_s. Thirdly, the presence of a temperature gradient results in an additional pressure-gradient-like term $-(\gamma-1)q$ in the momentum equation. This extra term produces an inwards directed force for a positive energy input $q > 0$, because the energy input heats the gas which reduces the outward temperature gradient and thus the outward force of the pressure gradient.

This momentum equation (16) has a singularity at the point where $v(r) = v_s$, this is called the *sonic point*. The numerator on the right hand side of the momentum equation is zero for $\gamma = 5/3$, when

$$\frac{e(r_c)}{r_c} + f(r_c) - \frac{2q(r_c)}{3} = 0 \tag{17}$$

in which $e(r)$ is defined by Eq. (13). This is the *critical point* of the adiabatic wind. If f and q are independent of $\mathrm{d}v/\mathrm{d}r$ like in the isothermal case the sonic point will coincide with the critical point. In general, however, f and g depend on $\mathrm{d}v/\mathrm{d}r$, which will produce additional terms on the left hand side of Eq. (16) so that the sonic and critical points no longer coincide.

Although equation (17) is a local condition, it depends on the energy and momentum input throughout the subsonic region because of the term $e(r_c)/r_c$.

2.2 What mechanism is driving the wind?

The phenomenon that stars loose mass is "ubiquitous across the Hertzsprung-Russell diagram"[3] , but their properties vary fundamentally. Stellar winds can be roughly divided into three classes: Hot star winds, coronal winds and cool non-coronal winds. These three classes are found in three disjunct regions in the Hertzsprung-Russell diagram, shown in figure 2. It is stressed that this classification is based on the differences in driving mechanism between the classes. The winds could equivalently be classified after observational characteristics [LH79] but such classifications have no application in the scope of this work.

2.2.1 Hot star winds

Hot star winds are found at the early type stars, earlier than B3. They typically have massive and high-velocity winds. Hot stars emit the bulk of their radiation in the ultraviolet where their outer atmospheres have many absorption lines. The opacity in absorption lines is much larger than the opacity in the continuum. The opacity of one strong line can easily be a factor of 10^6 larger than the opacity for electron scattering. Due to the Doppler shift from the high wind velocities, the atoms can be accelerated

[3]Deutsch 1968. Deutsch found the crucial evidence for mass loss from red giants 1956. The solar wind was observationally confirmed by the Mariner 2 interplanetary probe 1962.

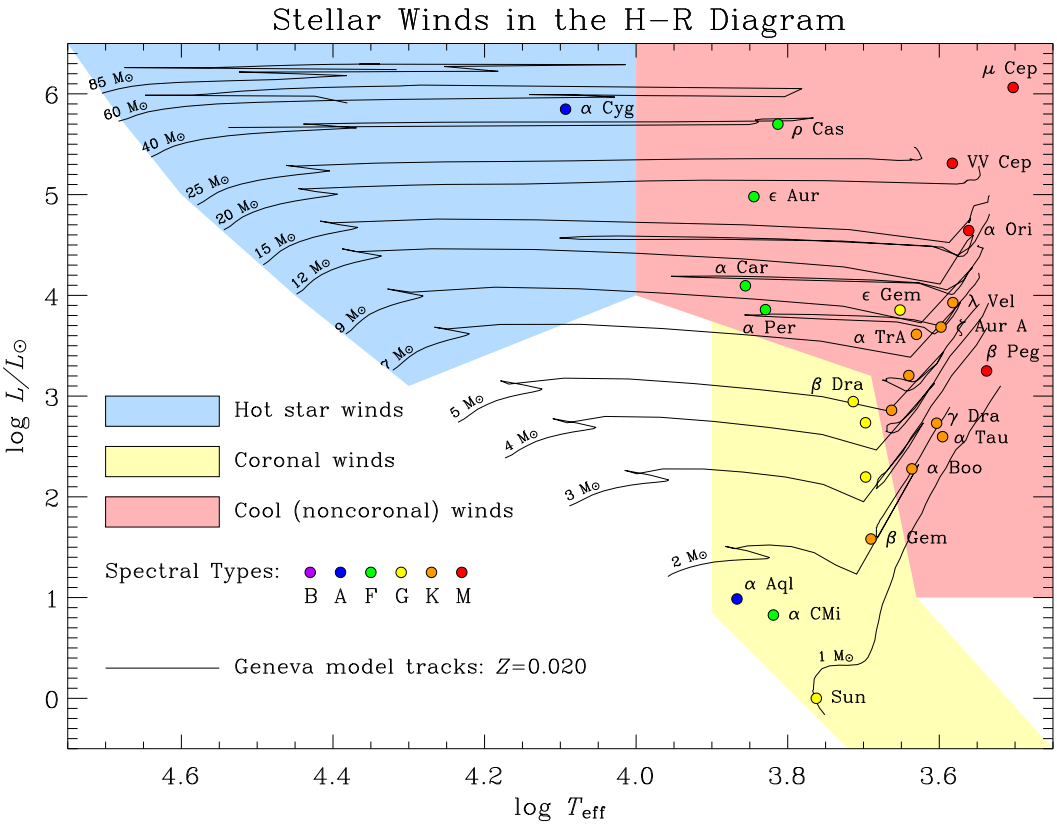

Figure 2: The locations of mass losing stars in the Hertzsprung-Russell diagram. The three classes of winds lie in the three shaded regions. The regions vary in the mechanism that drives the wind of a star in that region. (From [Ben05])

through the almost undiminished continuum radiation. This makes radiative acceleration due to spectral lines in the atmospheres of hot luminous stars a very efficient mechanism.

The main properties of this class of mass losing stars are:

$$\begin{aligned} 1000 \lesssim\ & v_\infty \lesssim 1500 \text{ km/s} \\ 10^{-8} \lesssim\ & \dot{M} \lesssim 10^{-4} M_\odot/\text{yr} \\ 2 \lesssim\ & \log g \lesssim 4 \end{aligned}$$

The basic mechanism that drives the hot winds is the *radiation pressure* on atomic lines. In principle this mechanism functions like an adiabatic wind with a pressure gradient force and gravity as only forces as described in section 2.1.2. To the gas pressure gradient the radiation pressure gradient is added. A more elaborate description of radiation driven winds can be found in [CAK75] [KPPA89] [Lam97].

2.2.2 Coronal winds

Main sequence stars later than about F0 V (and stars that have evolved off the main sequence and that have spectral types between F5 IV and about K1 III) are found to have tenuous, hot coronal winds. Whereas the temperature in the photosphere is about 6000K, in the outer layers of the atmospheres the temperature rises to several 10^6K. This region is called the corona. The temperature rise above the photosphere is due to the dissipation of mechanical energy or the reconnection of magnetic field lines that originate from the convection zone below the photosphere. Trapped coronal gas is heated until the thermal pressure approximately equals the magnetic pressure. The thermal pressure gradient induced by these processes is large enough to drive a Parker[4]-type wind.

The main properties of this class of mass losing stars are:

$$\begin{aligned} v_\infty &\approx 500 \text{ km/s} \\ \dot{M} &\approx 10^{-14} M_\odot/\text{yr} \\ \log g &\approx 4.5 \end{aligned}$$

The basic mechanism that drives the coronal winds is the *thermal pressure gradient*. This mechanism functions like an adiabatic wind with gas pressure and gravity as only forces (see section 2.1.2). However, there are some additional complications, like viscosity and thermal conduction, which transports heat from high temperature regions to low temperature regions. Other minor forces may play a role in the coronal holes, which are regions of lower temperatures and higher mass flux. For a more detailed description of coronal winds see [Bra70] [Par71] [LC99].

2.2.3 Cool winds

Evolved stars, later than about K1 of luminosity class III or higher, have cool, low-velocity, massive winds:

$$\begin{aligned} v_{g0} \gg \; v_\infty &\approx 40\text{km/s} \\ 10^{-8} \lesssim \; \dot{M} &\lesssim 10^{-4.5} M_\odot/\text{yr} \\ 0.5 \lesssim \log g &\lesssim 3 \end{aligned}$$

The mechanism of the previous class of winds, the thermal pressure gradient induced in the hot corona, can not be used to explain these winds.

[4]Parker was the first who proposed a hydrodynamic model. That model is still used for these winds, in which material flowed out of the sun as a natural consequence of the million degree temperature of the corona [Par58].

They are found to be far more massive than the coronal winds. And as the densities are much higher, the cooling process is more efficient. The heating process cannot compete with the cooling and no corona is developed. The mechanism of the hot winds is not applicable either, since the radiative flux is low and highly exitated atoms are absent. A number of other mechanisms have been proposed to drive gas out of the gravitational potential well of the star:

- sound waves from photospheric convection
- radiation pressure on dust grains
- atmospheric extension caused by shockwaves that originate from pulsations
- alfvén waves

but no mechanism nor a combination of mechanisms are known to be able to produce the observed effects [LB91] [Har96]. As will be shown in the next paragraph, it is natural that of all three types of wind this type is not yet fully understood.

2.3 Why the driving mechanism for cool winds is unknown

There are three reasons why for cool winds no mechanism has been found to meet the observational constraints. In order to identify the three problems, first the energy needed to drive the wind is considered. According to Eq. (13) the energy of the wind at radius r is

$$e(r) = \frac{1}{2}\left(v^2 - v_g^2 + \frac{2\gamma}{\gamma - 1} v_t^2\right) \tag{18}$$

The energy required to drive the wind from the base r_0 to r_∞ is

$$E_{0,\infty} = e(r_\infty) - e(r_0) \approx \frac{1}{2}\left(v_\infty^2 + v_{g0}^2\right) \tag{19}$$

which says that it is needed to lift the mass transported by the wind out of the stellar gravitational field and to accelerate the wind to its asymptotic velocity v_∞. For the approximation in Eq. (19) the following assumptions were used (they can be made for all three types of wind without loss of generality)

$$\begin{aligned} v_{g0}^2 &\gg v_0^2 + \frac{2\gamma}{\gamma - 1} v_{t0}^2 \\ v_\infty^2 &\gg \frac{2\gamma}{\gamma - 1} v_{t\infty}^2 \\ v_\infty^2 &\gg v_{g\infty}^2 \end{aligned} \tag{20}$$

These assumptions mean that the expanding atmosphere is gravitationally bound to the star and subsonic at the base r_0 and is highly supersonic at large distances, where the wind has achieves its asymptotic velocity.

At this point discrepancies arise between the three classes of winds. In the massive winds from early-type stars, for which $v_\infty^2 \gg v_{g0}^2$, virtually all of the driving energy of the wind goes into accelerating the flow to its asymptotic velocity. In solar-type winds, for which $v_\infty^2 \approx v_{g0}^2$, comparable parts of the winds's driving energy go into lifting the expanding atmosphere out of the stellar gravitational field and into accelerating it to the asymptotic flow velocity.

In the massive winds from low-gravity, late-type stars, for which $v_\infty^2 \ll v_{g0}^2$, almost all of the driving energy of the wind goes into lifting the expanding atmosphere out of the gravitational field. Here the *first problem* arises. For this implies, when considering the origin of the stellar wind one is dealing with only a small fraction of the total required energy ($v_\infty^2/(v_\infty^2+v_{g0}^2)$). One can thus expect to learn relatively little about the overall mass loss mechanism responsible for the mass loss, i.e. the forces that act in the subsonic region.

The energy required to drive the wind from the sonic point r_s to r_∞ is

$$E_{s,\infty} = \frac{1}{2}\left(v_\infty^2 + v_{gs}^2 - \left[\frac{2\gamma}{\gamma-1}+1\right]v_{ts}^2\right) \tag{21}$$

Generally in cool winds the adiabatic sound speed in the sonic point is not very high because of the low temperature of the wind, therefore the following approximation can be made

$$v_{g0}^2 \gg \left|v_{gs}^2 - \left(\frac{2\gamma}{\gamma-1}+1\right)v_{ts}^2\right| \tag{22}$$

Comparing (21) to (19) with the above approximation leads to the conclusion

$$E_{0,\infty} \gg E_{s,\infty} \tag{23}$$

A large fraction of the energy required to drive the wind must be added in the region of subsonic flow, and the small fraction added to the supersonic flow is tightly constrained by the required low asymptotic flow velocity. This is the *second problem*. For this constraint implies that the parameters of a wind model must be finely tuned. Fine tuning also complicates the application of the model to a broad range of stars. A solution to this problem could be a sort of atmospheric self-regulation mechanism that provides a physical basis for the fine tuning [HM85].

The *third problem* is related to the form of energy added to the wind. As mentioned before, a dense wind has an enormous cooling capacity through the emission of electromagnetic radiation. Therefore, the energy added to the wind must come in the form of momentum addition rather than heat addition, which is another restriction on the mechanism responsible for driving the wind.

2.4 Observing cool winds

There are two different ways to observe cool winds. The first method makes use of spectra of single stars, the second of spectra of binary systems containing a cool giant and a white dwarf.

2.4.1 Single star spectra

The structure of the wind of a single star can be examined from high resolution UV spectra. These contain many emission lines from singly ionised metal lines Fe II, Mg II, S II, C II and Al II. The formation depths of these lines span the range from the lower chromosphere to the regime of the terminal wind velocity, through the variety of optical thickness and excitation temperature.

The shape of the emergent line profile depends upon the local velocity fields in the line-forming regions. The location of the line forming region is determined by the *optical thickness*, which is the monochromatic line extinction coefficient α_λ, defined on page 28, integrated from the stellar radius R_* to the detector

$$\tau_\lambda^\star = \int_{R_*}^{r_\infty} \alpha_\lambda \mathrm{d}r \tag{24}$$

in which the stellar radius usually is defined as the radius r at which the optical depth (defined on page 28) τ_λ equals unity for some wavelength λ in the optical range of the spectrum.

$$R_* = r(\tau_\lambda = 1) \tag{25}$$

In figure 3 seven emission lines are shown for three cool stars with a stellar wind. The C II 2325.4Å line is formed in the chromosphere of the star. The wind does not influence the form of this line significantly because it is optically thin (see the text to figure 3) for this line. The Mg II 2802.7Å emission line is much broader and shows a self-reversed core, caused by absorption in the wind that is opaque in this line. The centre of the self-reversed core is blue shifted from the centre of the emission line formed in the chromosphere. The amount of this blue shift can be used to measure the asymptotic wind velocity. The five Fe II lines between the C II and the Mg II lines have optical thicknesses in the range between the C II and Mg II lines. As the line opacity increases, the emission component broadens in width and a self-reversal appears, which increases in strength and extends to higher blueshifts for higher opacity lines. β Gru has a denser wind than α Tau, as the effect of the self absorption for the β Gru lines is stronger than for the same lines in the α Tau spectrum. In α Boo the velocity of

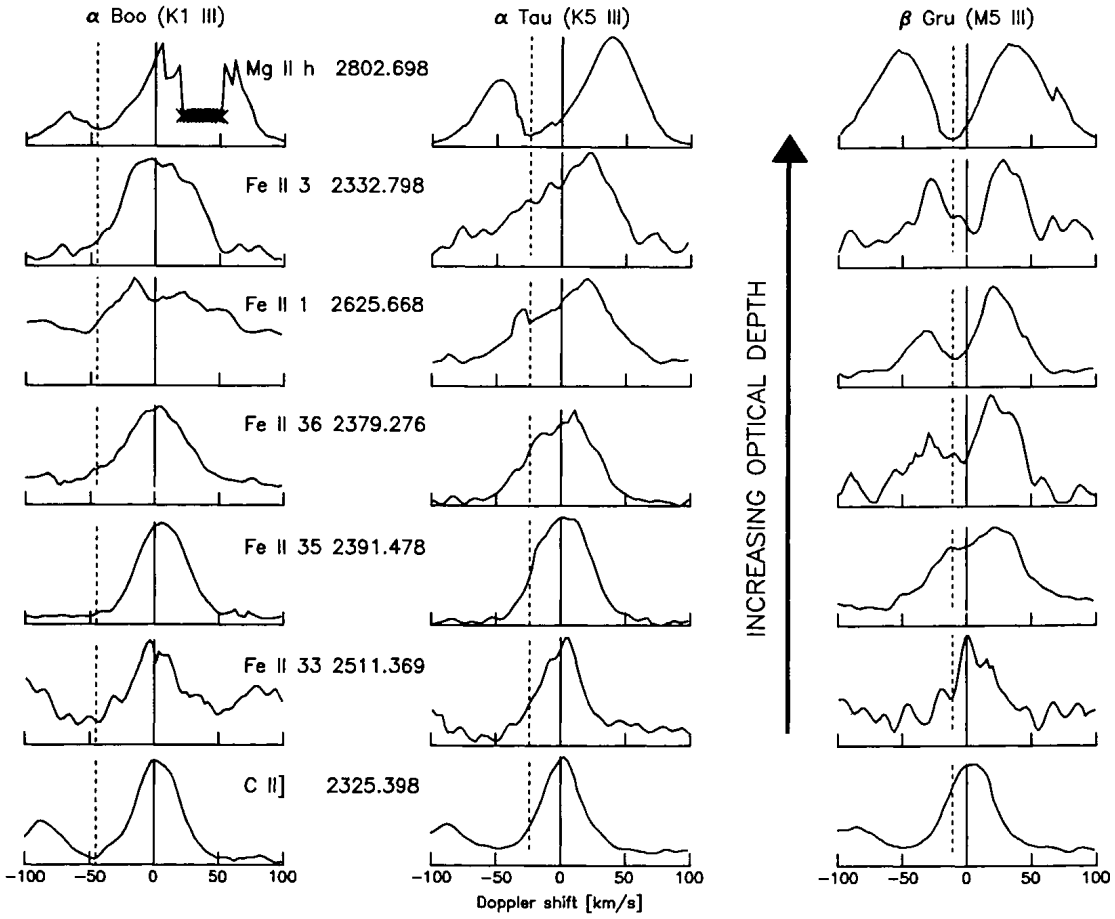

Figure 3: Typical line profiles of Fe II, C II, and Mg II in the spectra of two red giants(α Boo and α Tau) and a supergiant (β Gru), plotted against the Doppler shift. "Increasing optical depth" in this graph means increasing *optical thickness* $\tau^{\star}_{\lambda}$, defined in equation 24.
The terminal velocities of the stellar winds are determined from the Mg II lines and shown in the graphs as dotted lines. The Mg II lines are optically very thick so they are formed throughout the wind up to the regions of the asymptotic velocity. The C II line is optically very thin and is almost untouched by the wind. This line is used to find the center of the Doppler shift, due to the stellar radial velocity. The Fe II lines have thicknesses between those of Mg II and C II and can be used to determine the velocity in the lower regions, close to the stellar surface. (From [JJ91])

the wind is high enough so that all the emission lines of FeII are essentially unaffected by the presence of absorbing material in the wind.

By extracting the wind velocities for various heights above R_* the velocity field can be reconstructed. Another example of the variation the in line profile appearance with optical thickness found in the spectra of a the two red (super)giants γ Cru and λ Vel is shown in figure 4. The absorption core is stronger shifted with increasing optical line thickness.

Although this example of figure 4 illustrates the observational effect of higher blueshift at increasing formation height, the accurate reconstruction of a velocity field involves detailed model calculations [CRH$^+$99]. And because of the large number of parameters (e.g. temperature-, density-, and velocity-structure and metallicity) fits usually are not unique. Thus this method is prone to large inaccuracies.

Another problem with the observation of winds from single stars is that the emission lines in the UV are surrounded by numerous atomic lines so that high resolution spectra are needed to discern the specific lines and extract their profile. But cool giants are weak UV sources, so that only the closest brightest stars provide sufficient flux.

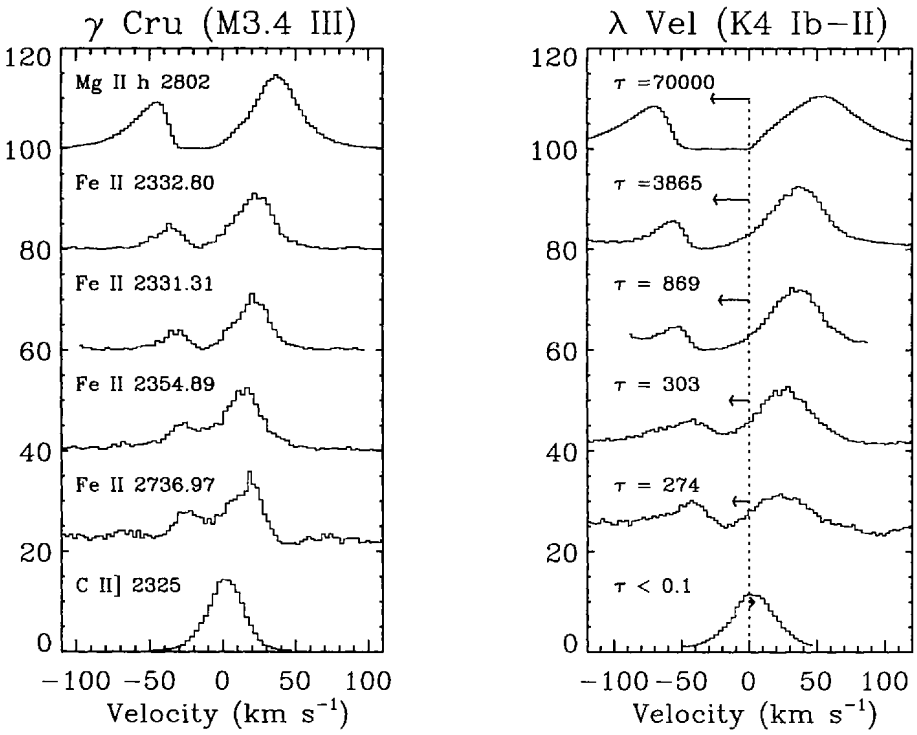

Figure 4: Typical emission line profiles that show a wind absorption core of a few singly ionised metal lines in the spectra of the two red supergiants γ Cru and λ Vel, plotted against the Doppler shift. In the left pane the line ID's are specified, in the right pane τ values are given. τ here stands for an estimated value[5] for the optical thickness $\tau^\star_\lambda$ defined in Eq. (24).
An arrow marks the apparent absorption core center, which is more blue shifted with increasing optical thickness. The shape of the thin lines, like C II 2325.4Å, comes mainly from the chromosphere, whereas the forming regions of the optically thicker lines extend to the outer layers of the wind. (From [BH97])

[5]The purpose of these values is to give an indication of the wind opacity for the absorption lines, as the actual opacity depends on the specific density and temperature structures. A rough approximation for the optical thickness of the wind $\tau^\star_\lambda$ can be made assuming an isothermal homogeneous wind with temperature T using the formula [CRH$^+$99]

$$\tau = \frac{\lambda_0}{1000}\, g f \exp\left(\frac{-\Delta E_l}{kT}\right)$$

where λ_0 is the rest wavelength of the line in Å, g is the statistical weight, f is the oscillator strength, ΔE_l is the excitation of the lower energy level, k is the Boltzmann constant.

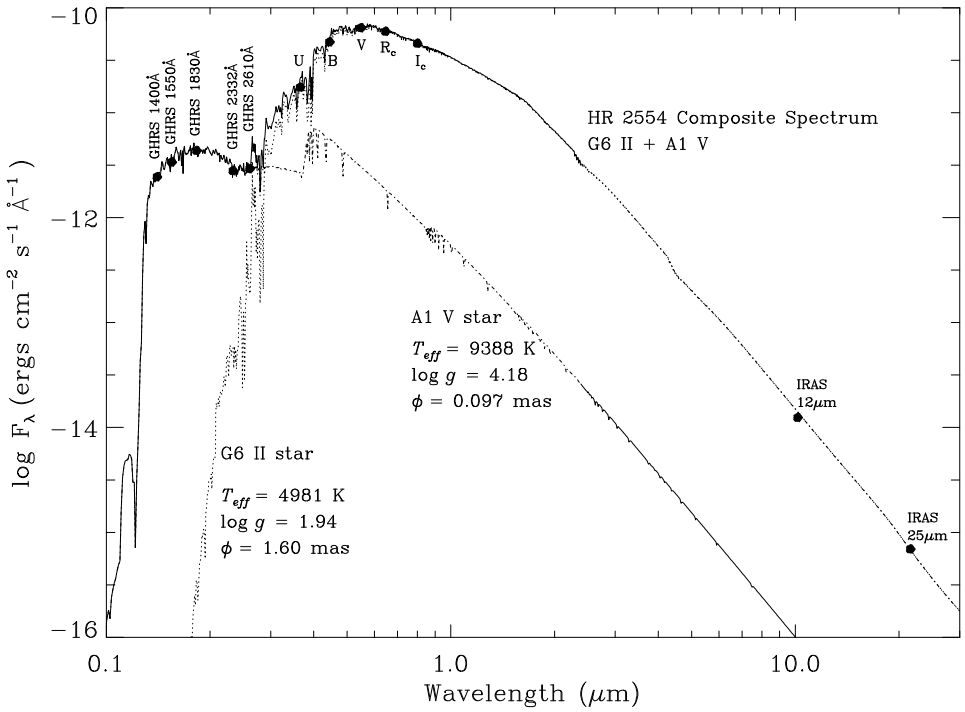

Figure 5: The spectral composition of a binary system. Although the G6 primary has a greater luminosity than the A1 companion, the UV spectrum is dominated by the companion. UV spectral lines are important for probing the wind, therefore the higher UV Luminosity of binaries is a great observational advantage over single stars. (From [BBB+01])

2.4.2 Binary systems

An alternative method to measure wind structures has been found by Deutsch (1956). It uses binary systems consisting of a cool supergiant primary that eclipses its dwarf companion. The secondary is much smaller than the primary and can be treated as a point source. The binaries are observed at high spectral resolution in the UV. The dwarfs are much brighter UV sources than the red supergiants, see figure 5, which makes them easier to detect than single red supergiants, and there is no need to deal with the disentangling of composite spectra.

Spectra taken at different orbital phases contain different spatial information, originating from different lines of sight through the primary's circumstellar shell, from the secondary on outward (see figure 6). When the secondary is in front of the primary the influence of the wind is at a minimum (the wind is far more extended than the binary separation). The spectrum changes when the secondary moves towards eclipse. For example, a resonance line appears in minimum absorption and gets stronger towards eclipse. During total eclipse the line turns into emission, as the photons

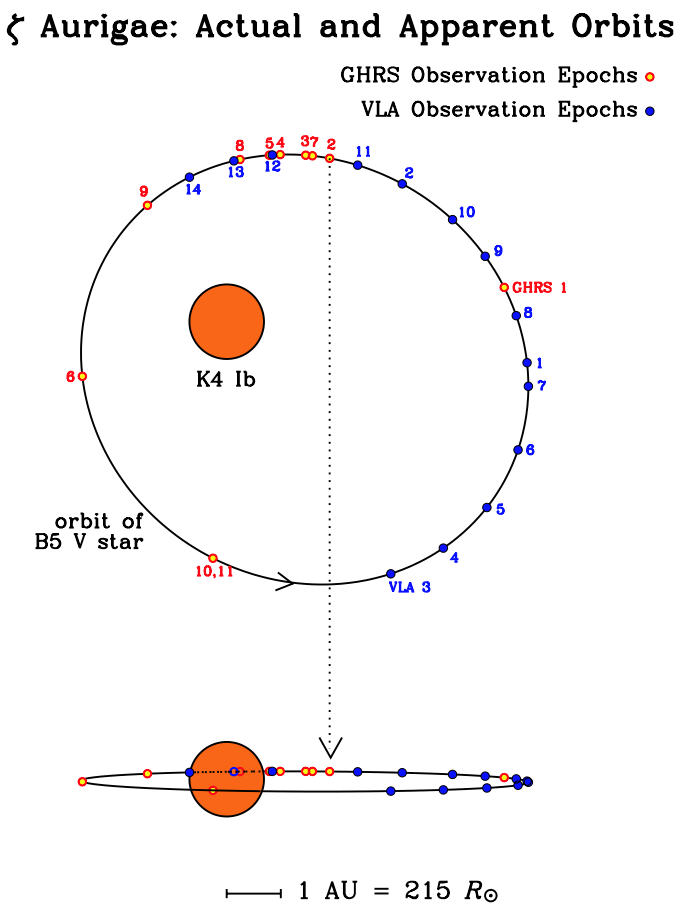

Figure 6: The actual and apparent orbit of the binary system ζ Aur. The line of sight, plotted as a dotted arrow, has its origin at the hot companion and is altered on its way to through the circumstellar envelope of the primary to the observer. Multiple high-resolution spectra for different orbital phases allow a reconstruction of the inner wind region through a kind of tomographic inversion. In the orbit of the companion the events are shown for two series of observations, one with the Hubble Space Telescope and the Goddard High Resolution Spectrograph and the other with the Very Large Array radio telescope. (From [HBB+05])

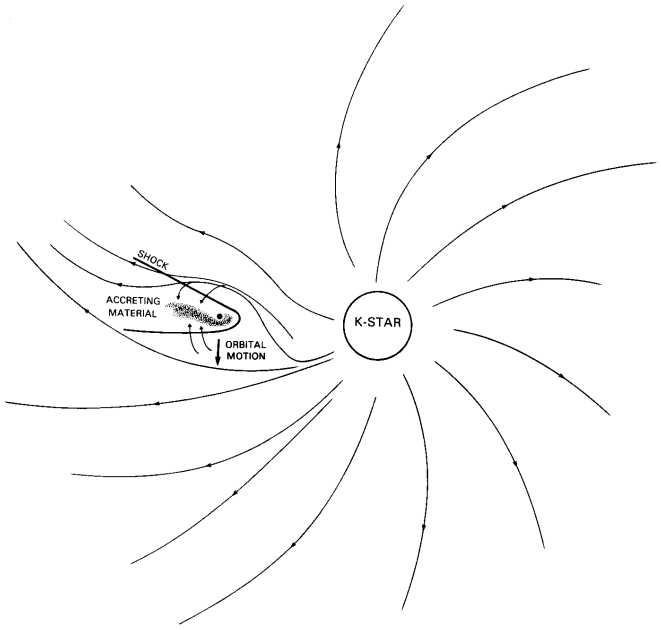

Figure 7: In a binary system the secondary moves with supersonic velocity through the circumstellar envelope of the primary. This produces a shockwave, that is expected have a considerable effect on the structure of the envelope. (From [Cha81])

from the hot star are scattered in the expanding envelope of the cool star.

From the changes in the spectrum the structure of the inner part of the wind region can be deduced. The outer regions, outside the orbit of the secondary, are reconstructed using the same methods as for single stars. Near eclipse, the secondary provides an opportunity to probe deep into the chromosphere. As explained in section 2.3, the wind acceleration in the subsonic region, at close distance to the primary, is responsible for the strength of the wind $\dot{M}$. Having tight observational constraints for the wind parameters is essential for finding a proper theoretical description of the wind driving mechanism.

But besides these advantages there is also a complication associated with the binary method. The question is to what extent the atmosphere and the wind (extended atmosphere) of the primary are influenced by the hot companion. The cool giant's atmosphere should be radiatively heated and gravitationally perturbed. The wind should be thinned out through accretion of matter on the secondary. The supersonic movement of the secondary through the wind should create a highly ionising shockwave, as shown in figure 7, and the secondary itself could also have a wind. The interaction of the two stellar winds should affect the velocity field considerably [HW82].

The precise impact of these influences is not known. There is only an

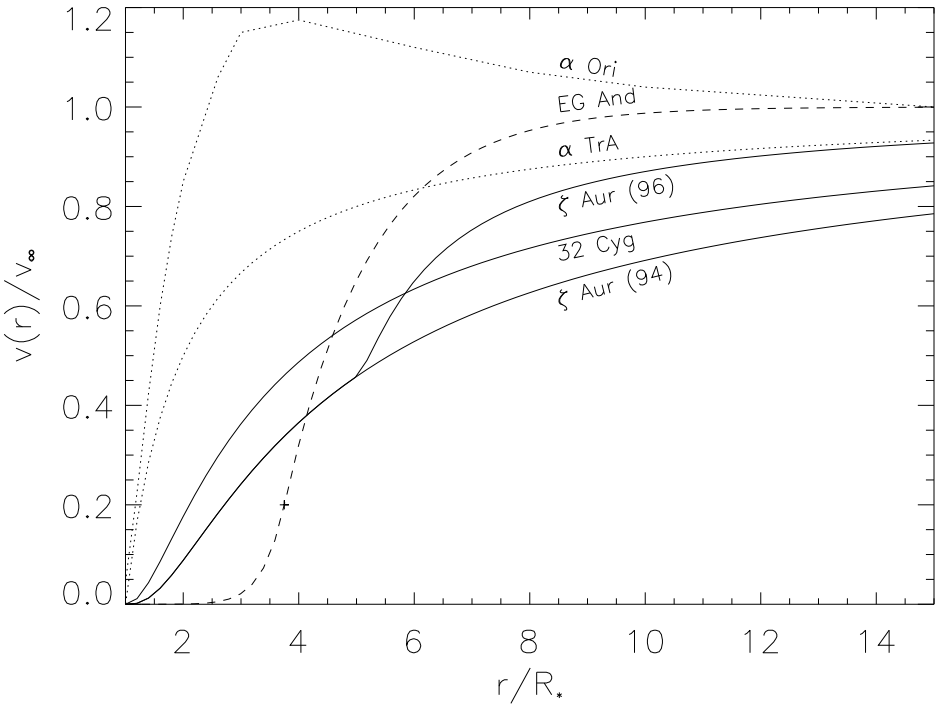

Figure 8: A collection of velocity profiles for different types of stars. The dotted lines are for single stars (α Ori [HA84] and α TrA [HDJB85]). The dashed line is a best fit for the symbiotic binary EG And [Vog91]. It contains a plus at the point where a power function changes into an exponential. The solid lines are for the binary systems 32 Cyg [Baa92] and ζ Aur which has two curves, one from 1994 [KB94] and an improved version from 1996 [BKR$^+$96]. Winds from the single stars seem to be stronger accelerated at a shorter range than those of the stars in binaries.

observational indication that at least the chromosphere of the primary is not strongly influenced by the secondary: the line profiles and fluxes of intrinsic chromospheric lines seem to show that chromospheres of supergiants in binaries are similar to those of single stars [Ben05].

2.5 Empirical velocity structures

The stars that feature cool stellar winds can clearly be divided into single stars and binaries. The wind structures that have been measured so far do show substantial differences, but also within these two classes. Besides being a binary or a single star there are apparently other stellar properties that affect the structure of the wind. In figure 8, six velocity structures are shown. All of these are results from semi-empirical model calculations. The two dotted curves show the most rapid acceleration and belong to *non-binary stars*. Such a rapid acceleration is confirmed for a number of single

stars, like α Boo, HD 6833 [DSL92] and six hybrid stars[6] [BM86]. For all these single stars, it is found that within one stellar radius distance from the star the wind is accelerated to half of its asymptotic velocity

$$v(r = R) = v_\infty/2 \qquad \text{for some} \quad R_* < R < 2R_* \tag{26}$$

The dashed curve of EG Andromedae shows fast acceleration too, but at a larger distance from the star ($\sim 3.75R_*$) than for the single stars. EG And is a *symbiotic binary*[7]. The accretion of matter has an obvious influence on the wind in addition to the effects mentioned in the previous paragraph. The wind velocity is below 10% of the terminal velocity at a distance of up to about $3.5R_*$. It is not clear from the source of this velocity field [Vog91] how R_* is defined. Possibly, the whole velocity field has to be shifted to the left to correct for an offset in R_*.

The three solid curves show velocity fields for winds from *binary stars* and exhibit a slower acceleration. Generally, all measured velocity fields of binary stars show a gradual acceleration

$$v(r = R) = v_\infty/2 \qquad \text{for} \quad R \approx 4R_* \tag{27}$$

different from the fields of single stars, see Eq. (26).

However, comparing velocity fields with a normalised radial distance, as in figure 8, can be misleading, as the wind acceleration mechanism is not proven to scale with R_*. Therefore, curves for super giants would appear much steeper than curves for similar winds from giants. In some cases the stellar radius was not accurately known when modelling the wind. For example, in 1981 the wind of α TrA has been determined for two cases of stellar parameters, $R_* = 157R_\odot$ and $R_* = 277R_\odot$ [HDR81]. In 1985 for the same star a value of $R_* = 97R_\odot$ has been used [HDJB85]. But as the velocity fields are results from model calculations that depend on R_*, one can not simply rescale the field with a factor $R_{*,new}/R_{*,old}$.

Furthermore, the uncertainties in these curves are considerable. And as the observational data get better, the models allow a more precise determination of the wind velocity. An example is shown in figure 8, in which there is a curve for ζ Aur from 1994 and an improved one that was made two years later.

[6]Hybrids are cool giants and supergiants featuring "warm" emission lines in their UV spectra and massive cool winds. With the term warm is meant a temperature of $4.2 \lesssim \log T \lesssim 5.2$. In the sun such temperatures occur in the transition region between the chromosphere and the "hot" corona ($\log T \approx 6$). Hybrids do not emit detectable X-ray flux, so obviously there is a negligible amount of "hot" gas in the atmosphere.

[7]Symbiotic binaries are long period binary systems with three typical constituents: a cool component, a hot component and a gaseous nebula surrounding the binary. In the type considered here a white dwarf accretes matter lost as stellar wind by a cool (super-)giant.

2.5.1 The β-Law

A common velocity parametrisation used to fit the data is the β power-law

$$v(r) = v_0 + (v_\infty - v_0)\left(1 - \frac{r_0}{r}\right)^\beta \tag{28}$$

Usually r_0 is taken to be the stellar radius R_*[8] and v_0 a small fraction of the asymptotic velocity. Often the simpler form

$$v(r) = v_\infty \left(1 - \frac{R_*}{r}\right)^\beta \tag{29}$$

is used, which is a good approximation except for radii very close to R_*.

This β-law originates from the line driven winds from hot stars, where the analytic solution is a β-law[9] with $\beta = 1/2$.

The curves for α TrA, 32 Cyg and ζ Aur (94) in figure 8 are β-laws with $\beta = 1.0$, $\beta = 2.5$ and $\beta = 3.5$ respectively. The curve for ζ Aur (96) consists of two consecutive β-laws, the first is for $R_* < r < 5R_*$ and has $\beta = 3.5$, the second is for $r > 5R_*$ and has $\beta = 1.5$ [BKR$^+$96]. This steeper slope at a larger distance from the star is supported by the observations from EG And, shown in that same figure 8.

2.6 Why modelling cool winds with `PHOENIX`

A complete self-consistent theoretical description for the mechanism driving cool winds has not been established yet. Therefore, the observational constraints on the theory need to be improved to provide a better basis for theoretic considerations. The processes that are involved in forming the spectrum take place in different stationary and expanding regions. An accurate reconstruction of the physical conditions at these locations is required to further increase the amount of information that can be obtained from the spectra. This implies, that model atmosphere calculations need to be most rigorous and realistic.

One of the most advanced model atmospheres that is capable of calculating expanding atmospheres is `PHOENIX` [HB98]. `PHOENIX` is a general-purpose state-of-the-art stellar atmosphere code with the following features:

1. 1D spherical symmetric radiative transfer
2. expanding media
3. the radiative transfer equation is solved using operator splitting
4. the NLTE rate equations are solved using operator splitting techniques

[8] Formally this is not correct, because r_0 is the radius at which the wind has a velocity v_0, whereas R_* is defined via the optical depth (Eq. (25)).

[9] in the assumption that the radiation pressure is much larger than the gas pressure, which is a rather good approximation for typical hot winds.

5. usage of four atomic databases with NLTE transitions: CHIANTI Version 3 and 4, APED (ATOMDB) and the Kurucz database
6. line blanketing and background opacities are included by design
7. over 650 species in the EOS including atoms, ions, molecules and grains
8. dynamical opacity sampling (dOS) of about 42 Million atomic lines and over 550 Million (and growing) molecular lines (more than 10GB worth of data)
9. spectra can be calculated for any desired resolution (standard are 20000 to 500000 wavelength points spread from the UV to the radio)

`PHOENIX` has been used to model hot winds before [Auf00], but not for cool winds. In the following chapter some aspects of `PHOENIX` are explained which are important for the cool wind modelling process.

3 The PHOENIX code for expanding atmospheres

The modelling process for cool winds can be divided into three steps. At first, an initial atmospheric structure is setup. Then, the radiation transport is calculated. Finally, the constructed atmosphere is corrected for deviations from the conservation of energy. In this section, first the two latter (general) modelling steps are explained (the radiative transport and the temperature correction method), so an atmospheric structure is assumed to be already available. Afterwards the (wind specific) atmosphere setup process is described. For this step a piece of code is used written for the construction of hot-wind atmospheres [Auf00].

3.1 Radiative transfer

Before discussing how radiation is transported through an atmosphere and how the transport equation can be solved numerically, some definitions of radiation related quantities are given.

3.1.1 Basic definitions

The definitions given here comprise only some of the most important radiation quantities, namely those which are needed for the following sections. It is mainly a summary of [RL79]. Another useful description of the processes that form and affect the light a star emits is given in [Rut95].

Intensity The specific intensity (or surface brightness) I_ν is the proportionality coefficient in:

$$\mathrm{d}E_\lambda \equiv I_\lambda(\vec{r},\vec{l},t)(\vec{l},\vec{n})\,\cos\theta\,\mathrm{d}A\,\mathrm{d}t\,\mathrm{d}\lambda\,\mathrm{d}\Omega \tag{30}$$

with $\mathrm{d}E_\nu$ the amount of energy transported through the area $\mathrm{d}A$ at the location $\vec{r}$, with $\vec{n}$ the normal to $\mathrm{d}A$, between times t and $t+\mathrm{d}t$, in the frequency band between ν and $\lambda+\mathrm{d}\lambda$, over the solid angle $\mathrm{d}\Omega$ around the direction $\vec{l}$ with polar coordinates θ and ϕ. This is the monochromatic intensity. The total intensity $I=\int_0^\infty I_\nu\,\mathrm{d}\lambda$.

Emissivity The contribution of the local monochromatic emissivity η_λ (defined per cm^3) to the intensity of the beam is

$$\mathrm{d}I_\lambda(s) \equiv \eta_\lambda(s)\,\mathrm{d}s \tag{31}$$

where s measures the geometrical path length along the beam in cm.

Extinction coefficient The monochromatic extinction coefficient χ_λ specifies the energy fraction taken from a beam per unit path length (actually a geometrical cross-section per unit volume ($\mathrm{cm}^2 \cdot \mathrm{cm}^{-3} = \mathrm{cm}^{-1}$)).

$$\mathrm{d}I_\lambda \equiv -\chi_\lambda I_\lambda \, \mathrm{d}s \tag{32}$$

Source function The source function is the ratio of the previous two quantities

$$S_\lambda \equiv \eta_\lambda / \chi_\lambda \tag{33}$$

Optical depth The optical depth is defined as

$$\mathrm{d}\tau_\lambda \equiv -\chi_\lambda \, \mathrm{d}s \tag{34}$$

This definition is valid for any line of sight. In this work, however, the radial optical depth is used

$$\tau_\lambda(r) = \int_r^\infty \chi_\lambda(r) \, \mathrm{d}r \tag{35}$$

which measures the optical depth along the radial line of sight from $\tau_\lambda = 0$ at the observer's eye located at $r = \infty$ through the center of the star at $r = 0$.

The radiative transfer equation The rate of change of the intensity of a beam is given by the combined effects of emission (Eq. (31)) and extinction (Eq. (32))

$$\frac{\mathrm{d}I_\lambda}{\mathrm{d}s} = \eta_\lambda - \chi_\lambda I_\lambda \tag{36}$$

This basic equation expresses that photons do not decay spontaneously so that the intensity along a ray does not change unless photons are added to the beam or taken from it.

3.1.2 The spherical symmetric radiative transfer equation

The radiative transfer equation (36) for the case of a spherically symmetric atmosphere (SSRTE) for a co-moving frame can be written as [MW84] [HB98]

$$\alpha_r \frac{\partial I_\lambda}{\partial r} + \alpha_\mu \frac{\partial I_\lambda}{\partial \mu} + \alpha_\lambda \frac{\partial}{\partial \lambda} (\lambda I_\lambda) + 4\alpha_\lambda I_\lambda = \eta_\lambda - \chi_\lambda I_\lambda \tag{37}$$

with the three functions to ease the notation

$$\begin{aligned}
\alpha_r &= \gamma(\mu+\beta) \\
\alpha_\mu &= \gamma(1-\mu^2)\left[\frac{1+\beta\mu}{r} - \gamma^2(\mu+\beta)\frac{\partial\beta}{\partial r}\right] \\
\alpha_\lambda &= \gamma\left[\frac{\beta(1-\mu^2)}{r} + \gamma^2\mu(\mu+\beta)\frac{\partial\beta}{\partial r}\right]
\end{aligned}$$

and the following variables

$I_\lambda(r,\mu)$: specific intensity
r : radial coordinate
μ : cosine of the direction angle, $\mu = \cos\theta$
v : velocity, $\beta = v/c$, $\gamma^2 = 1/(1-\beta^2)$
$\chi_\lambda(r)$: extinction coefficient, $\chi = \kappa + \sigma + \sigma_l\varphi_l(\lambda)$, with κ the absorption coefficients, σ the scattering coefficients for continuum processes, σ_l the line scattering coefficients and φ_l the line profile function.
$\eta_\lambda(r)$: emissivity

On the right hand side of Eq. (37), η_λ contains contributions from scattering terms of the continuum and spectral lines.

$$\eta_\lambda = \kappa_\lambda B_\lambda(T) + \sigma_\lambda J_\lambda + \sum_{\text{lines}} \sigma_{l\lambda} \int_0^\infty \varphi(\lambda) J_\lambda \,\mathrm{d}\lambda \tag{38}$$

κ_λ : absorption coefficient
σ_λ : scattering coefficient for continuum processes
$\sigma_l(\lambda)$: line scattering coefficient
$\varphi_l(\lambda)$: line profile function
S_λ : source function
J_λ : mean intensity

The mean intensity J_λ is the zeroth angular moment of I_ν

$$J_\lambda = \frac{1}{2}\int_{-1}^{1} \mathrm{d}\mu I_\lambda \tag{39}$$

The basic problem of radiative transfer is that the evaluation of a particular $I_\lambda(\tau_\lambda,\mu)$ requires S_λ, and therefore J_λ, and therefore I_λ in many directions, and therefore S_λ at many locations and many wavelengths. With equation (38) the SSRTE becomes an integro-differential equation. It is time independent and the velocity field is monotonic. Thus the SSRTE becomes a boundary value problem in spatial coordinates and an initial value problem in wavelength coordinates. The SSRT equation (37) is solved with the Accelerated Lambda Iteration (ALI) method as described in [Hau92] and [HB04].

3.1.3 The Accelerated Lambda Iteration

In order to solve the radiative transfer problem J_λ is calculated via the source function S_λ by a formal solution of the SSRTE by using the so called Lambda operator Λ_λ

$$J_\lambda = \Lambda_\lambda S_\lambda \tag{40}$$

The usual Lambda iteration method

$$J_{\text{new}} = \Lambda S_{\text{old}} \tag{41}$$
$$S_{\text{new}} = (1-\epsilon)J_{\text{new}} + \epsilon B \tag{42}$$

fails in the case of large optical depths and small ϵ (thermal coupling parameter, B is the Planck function). The range of the Lambda operator is only in the order of $\Delta\tau \sim 1$. At large optical depths, the mean intensity calculated with the Lambda iteration must be $J_\lambda = B_\lambda + O(e^{-\tau_\lambda})$ and the convergence is infinitely slow. If there are high opacities in certain wavebands, J_λ is equal B_λ and the convergence is too slow again.

Therefore, an approximate Lambda Operator Λ^* is used, which is defined by

$$\Lambda = \Lambda^* + (\Lambda - \Lambda^*) \tag{43}$$

Thus equation (40) can be written as

$$J_{\text{new}} = \Lambda^* S_{\text{new}} + (\Lambda - \Lambda^*) S_{\text{old}} \tag{44}$$

and from equation (42) then follows

$$[1 - \Lambda^*(1-\epsilon)]\, J_{\text{new}} = J_{\text{fs}} - \Lambda^*(1-\epsilon) J_{\text{old}} \tag{45}$$

where $J_{\text{fs}} = \Lambda S_{\text{old}}$ is the formal solution. With equations (43) - (45) new values of the mean intensity J_{new} can be obtained and with equation (42) the new source function can be calculated. The new problem is to compute the approximate Lambda Operator Λ^*.

3.1.4 Computation of the approximate Lambda Operator

For a fast computation of equation (45) the calculation and structure of Λ^* should be simple. Fastest convergence is obtained with $\Lambda = \Lambda^*$ but to construct Λ is more time consuming than to construct a simpler Λ^*. The diagonal or tri-diagonal form of the exact Λ matrix is optimal for a fast convergence and computation of Λ^*.

The formal solution is performed along characteristic rays [OK87]. Along the characteristic rays the SSRT Eq. 37 has the form [Mih80]

$$\frac{\partial I}{\partial s} + \alpha_\lambda \frac{\partial \lambda I}{\partial \lambda} = \eta - (\chi + 4\alpha_\lambda) I \tag{46}$$

where s is the geometrical path length along a ray. In an expanding medium the characteristic rays are curved. Before the SSRTE can be solved these have to be calculated. The source function is interpolated piecewise linearly or parabolically along each ray. For the specific intensity $I(\tau_i)$ the following expressions are obtained along a ray k

$$I^k(\tau_i^k) = I^k(\tau_{i-1}^k)\exp(\tau_{i-1}^k - \tau_i^k) + \int_{\tau_{i-1}^k}^{\tau_i^k} \hat{S}(\tau)\exp(\tau - \tau_i^k)\mathrm{d}\tau \quad (47)$$

$$I_i^k \equiv I_{i-1}^k \exp(-\Delta\tau_{i-1}^k) + \Delta I_i^k \quad (48)$$

τ_i^k is the optical depth along the ray k with i as the running index of the optical depth points. With $\tau_1 = 0$ and $\tau_{i-1}^k \leq \tau_i^k$ it follows for the calculation of τ^k:

$$\Delta\tau_{i-1}^k = (\hat{\chi}_{i-1} + \hat{\chi}_i)|s_{i-1}^k - s_i^k|/2 \quad (49)$$

$\hat{\chi}_i = \chi_i + 4\alpha_{\lambda,i}$ is the effective extinction coefficient at point i and $|s_{i-1}^k - s_i^k|$ is the geometrical path length between point i and $i-1$ along the ray k.

For ΔI_i^k the following expression applies

$$\Delta I_i^k = \alpha_i^k \hat{S}_{i-1} + \beta_i^k \hat{S}_i + \gamma_i^k \hat{S}_{i+1} \quad (50)$$

α_i^k, β_i^k, and γ_i^k are interpolation coefficients. When computing this coefficients it has to be distinguished between parabolic and linear interpolation of the source function $\hat{S}$. The expressions for the coefficients can be found in equations (23) to (25) in [Hau92] and in [HB04].

The Λ^* operator can be split up into two parts

$$\Lambda^* = \Lambda^t + \Lambda^c \quad (51)$$

Λ^t is the part for rays tangential to the core and Λ^c for core intersecting rays. Equations to compute the parts of Λ^t and Λ^c are in equations (27) to (32) of [Hau92]. With these equations it follows for the expression of the full Λ-matrix

$$\Lambda_{ij} = \sum_k \left(\sum_l w_{l,j}^k \lambda_{l,j}^k + \sum_{l'} w_{2(k+1)-l',j}^k \hat{\lambda}_{2(k+1)-l',j}^k \right) \quad (52)$$

$w_{i,j}^k$ are the angular quadrature weights, $\{l\}$ is the set $\{i \leq k+1\}$, and $\{l'\}$ is the set $\{i > k+1\}$. The coefficients $\lambda_{l,j}^k$ and $\hat{\lambda}_{l,j}^k$ depend on the interpolation coefficients α_i^k, β_i^k, and γ_i^k. How many coefficients have to be computed depends on the bandwidth of the Λ-matrix. The CPU time required for a computation of the full Λ-matrix can be reduced with a smaller bandwidth.

3.2 The temperature correction method

At the end of each iteration the temperature structure is checked to satisfy the energy conservation, equation (72). In order to correct the deviations from exact energy conservation a temperature correction procedure is applied. In the calculation of expanding atmospheres a generalization of the Unsöld-Lucy temperature correction scheme to spherical geometry is used [HBBA03].

The Unsöld-Lucy correction works on the principle that the ratios of mean opacities κ_P, κ_J and κ_F depend much less on changes in the temperature structure than the integrated properties of the radiation field J_λ, F_λ and K_λ. To obtain radiative equilibrium, the Planck function B has to be corrected

$$\begin{aligned}\Delta B(r) &= \frac{1}{\kappa_P}\{\kappa_J J - \kappa_P B + \dot{S}/(4\pi)\} - \{2(H(\tau=0) - H_0(\tau=0)) \\ &\quad - \frac{1}{fqr^2}\int_r^R qr'^2 \chi_F (H(r') - H_0(r'))\mathrm{d}r'\} \end{aligned} \tag{53}$$

with

$$\begin{aligned}\kappa_P &= \left(\int_0^\infty \kappa_\lambda B_l \mathrm{d}\lambda\right)/B \\ \kappa_J &= \left(\int_0^\infty \kappa_\lambda J_l \mathrm{d}\lambda\right)/J \\ \chi_F &= \left(\int_0^\infty \chi_\lambda F_l \mathrm{d}\lambda\right)/F \end{aligned}$$

as the wavelength-averaged absorption and emission coefficients. B is the Planck function, J is the mean intensity, and F is the radiation flux. $H = F/4\pi$, $H_0(\tau)$ is the target luminosity, and q is the sphericity factor

$$q = \frac{1}{r^2}\exp\left(\int_{r_{core}}^r \frac{3f-1}{r'f}\mathrm{d}r'\right) \tag{54}$$

where r_{core} is the inner radius. R is the outer radius of the atmosphere. $f(\tau) = K(\tau)/J(\tau)$ is the Eddington factor with $K = \frac{1}{2}\int \mu^2 I \mathrm{d}\mu$ as the second angular moment of the intensity I. $\dot{S}$ is the sum over all additional sources of energy, e.g. mechanical energy. The first term of equation (53) is dominant in the outer parts of the atmosphere and the second term in the inner parts.

Once ΔB is known, the temperature correction follows from the Stefan-Boltzmann law

$$\Delta T(r) = \frac{\mathrm{d}T}{\mathrm{d}B}\,\Delta B = \frac{\Delta B(r)}{4\sigma_{\mathrm{SB}} T^3(r) r^2} \tag{55}$$

where σ_{SB} is the Stefan-Boltzmann constant.

3.3 The hot-wind model: construction of the extended atmosphere

`PHOENIX` contains a wind model that was constructed by J. Aufdenberg [Auf00] for the purpose of modelling hot-winds.

The gas escaping from a star in an ideal case is treated as a hydrodynamic flow, satisfying the conservation of mass, momentum, and energy. But in sections 2.2.3 and 2.3 the problems have been shown inherent in constructing a self consistent theoretical model based on

1. the two fundamental equations: the continuity equation (1) and the momentum equation (16)
2. the lower boundary conditions ρ_0, v_0, v_{g0} and T_0

that is to satisfy the upper boundary conditions at r_∞. Now as no self-consistent model is known that produces results in agreement with the most basic observational data one has to fall back on semi-empirical models.

In the model the atmosphere is strictly divided into a hydrodynamic (wind) region and a hydrostatic region.

3.3.1 Wind region

In a semi-empirical model the momentum equation is not used to calculate the velocity structure, so *momentum conservation* is no longer enforced. But mass and energy conservation is yet presumed. The continuity equation

$$\dot{M}(r) = 4\pi r^2 \rho(r) v(r) = \dot{M} \tag{56}$$

represents *mass conservation*, and is used to fix the density structure

$$\rho(r) = \frac{\dot{M}}{4\pi r^2 v(r)} \tag{57}$$

in which $v(r)$ is an empirical velocity field, a β-law is the best candidate at present (see section 2.5)

$$v(r) = v_\infty \left(1 - \frac{R_*}{r}\right)^\beta \tag{58}$$

In contrast to Eq. (28) this common form of the β-law that is implemented in the model requires that $r > R_*$ for the base of the hydrodynamic region, to prevent $\rho(r)$ from going to infinity there.

The energy conservation is used after the atmospheric structure is setup to iteratively refine the model. When the *energy conservation* equation (72) has reached its prescribed accuracy, then the model is converged. This process is described in section 3.2.

The structure of the dynamic layers is computed on a fixed radial grid. The structure of the static layers of the atmosphere is computed on an optical depth grid. Typically 50 layers are used consisting of 35 layers for the wind region and 15 layers for the static region. The radial grid points are prescribed by a cosh-law to finely sample the inner region of the wind, where the velocity gradient is steepest, and to coarsely sample the outer portion of the wind where the velocity gradient is small.

The radii $r(l)$ in the upper layers $l = 1, \ldots, l_*$ are specified by

$$r(l) = R_{\min} + R_{\max} \frac{\cosh\left(C\frac{l_*-l}{l_*}\right) - 1}{\cosh\left(C\frac{l_*-1}{l_*}\right)} \tag{59}$$

where l_* is the layer immediately above the dynamic-static transition, typically layer 35, and C is a constant (typically $C > 5$) that can be used to adapt the radial sampling to the form of the velocity field. Equation (59) does satisfy $r(l_*) = R_{\min}$, but $r(l = 1) = R_{\max}$ generally not. This issue is returned on in section 4.4.2 on page 46. Layer 1 is the outermost layer and typically we choose the radial extension in the wind to be a factor of 200, $r(l = 1) = 200R_*$. The radius of the layer above the transition radius $r(l_*)$ is defined as

$$R_{\min} = \frac{R_*}{1 - \left(\frac{v_{\min}}{v_\infty}\right)^{1/\beta}} \tag{60}$$

with

$$v_{\min} = p_{\min} \cdot v_\infty \tag{61}$$

a percentage of the terminal velocity. The default value of $p_{\min} = .002$.

The optical depth scale $\tau_{\rm std}(l)$ is obtained from the radial scale $r(l)$ by integrating

$$\mathrm{d}\tau_{\rm std} = -\kappa_{\rm std}\rho\,\mathrm{d}r \tag{62}$$

where $\mathrm{d}\tau_{\rm std}$ and $\kappa_{\rm std}$ are the optical depth and mass extinction coefficient respectively, both at the reference wavelength $\lambda_{\rm std} = 12000$Å. κ is calculated

for each layer from the pressure and the temperature using the equation of state

$$\kappa(l) = \kappa(P_g(l), T(l)) \tag{63}$$

where the gas pressure $P_g(l)$ is calculated with with the ideal gas law

$$P_g = \frac{\rho k T}{\mu m_H} \tag{64}$$

with $\mu \equiv \bar{m}/m_H$ the mean "molecular" weight per free particle (including free electrons) in atomic units, and $P_g = \sum_i P_i = \frac{\rho k T}{m_i}$ the gas pressure is the sum of all partial pressures, with i specifying all types of particles including free electrons. The density $\rho(l)$ needed in Eq. 64 was available already (Eq. 57), a temperature structure $T(l)$ is specified as input parameter $T^{(0)}(l)$.

3.3.2 Hydrostatic region

In the hydrostatic layers ($l = l_* + 1, \ldots, N$) the structure is computed on a fixed logarithmically spaced optical depth grid

$$\log(\tau(l)) = \log(\tau(l_*)) + (l - l_*) \left[\frac{\log(\tau(N)) - \log(\tau(l_*))}{N - l_*} \right] \tag{65}$$

starting from the value of the dynamic region's bottom layer $\tau(l_*)$. Here $\tau = \tau_{\rm std}$ to ease the notation. From here on for all occurrences of τ referring to the optical depth grid $\tau = \tau_{\rm std}$ holds. The lower boundary is defined for an optical depth $\tau(N) = \tau_{\rm max}$ with a typical value[10] of $\tau_{\rm max} = 100$ to ensure it is set well below the thermalisation depth[11].

Once the complete τ-grid is available the temperature structure, that is supplied as input parameter $T^{(0)}(\tau)$, is mapped onto the new grid by interpolation.

Now the complete atmospheric structure can be computed for each layer by numerically integrating the hydrostatic equation

$$\frac{{\rm d}P_g}{{\rm d}\tau_{\rm std}} = -\frac{g}{\kappa_{\rm std}} \tag{66}$$

downwards, starting from the transition layer l_* at which the pressure, density and thus the mass extinction coefficient are already known. The radius for every layer is calculated using equation (62).

[10] The value of 100 says that only e^{-100} of the radiation field at that depth in the atmosphere is not absorbed on its way out to the observer by absorption processes.

[11] The thermalisation depth is defined as the optical depth at which the radiation field "thermalises" $J_\lambda = B_\lambda$ as seen from outside. It is not easy to pin down the exact location at which this is satisfied, therefore mostly a thermalisation proximity is meant.

3.3.3 Structure check

When the complete atmosphere is constructed the radial grid is checked and if necessary adjusted so that the the jump in the density is smooth across the static/dynamic transition, that is when

$$\Delta_B \equiv \rho(l_* + 1)/\rho(l_*) < 5 \tag{67}$$

If the ratio is larger than 5 a new target value for the bottom wind layer density

$$\rho'_* = \rho(l_* + 1)/2 \tag{68}$$

is set and then the setup is repeated from the beginning, starting with the radial grid setup, in which $v_{\min}$ this time is not set as a percentage of the terminal velocity (Eq. (61)), but by

$$v_{\min} = v_{\min} \frac{\rho(l_*)}{\rho'_*} < \frac{2}{5} v_{\min} \tag{69}$$

where for the last step equations (67) and (68) are used.

Once this smoothness requirement is fulfilled the next higher density jump is checked, which should satisfy

$$\Delta_A \equiv \rho(l_*)/\rho(l_* - 1) < 5 \tag{70}$$

If this is not met, the input parameter C is increased in small steps

$$C = C + \frac{1}{10} \tag{71}$$

The slope of the radial grid lowers for small r and rises for high r, thus the bottom of the wind region is finer sampled. Again, the complete atmospheric structure is recomputed, now with the new value for C. The requirements for Δ_A and Δ_B both have to be fulfilled within 10 iterations, otherwise the grid construction is halted. Better starting values for C and $p_{\min}$ must then be set in order to successfully complete the model.

In fact, the new target density ρ'_* is also set when Δ_A is found to be too large. This leads to problems when calculating cool winds. This problem is described in section 4.5 on page 47.

3.4 Model completion

Once a proper atmospheric structure is found for all layers, the radiative transfer problem is solved, which is described in section 3.1.2. Then the

temperature structure is iteratively corrected using the temperature correction scheme (see page 32) to improve energy conservation. The energy conservation is specified in the Lagrangian frame by *radiative equilibrium*

$$\int_0^\infty (\eta_\lambda - \chi_\lambda J_\lambda)\,\mathrm{d}\lambda \leq \varepsilon \tag{72}$$

where η_λ and J_λ describe the emissivity and mean intensity respectively and $\varepsilon = 0$ for exact radiative equilibrium, when each element of material absorbs exactly the same amount of energy that it emits. In the modelling process exact equilibrium is not forced but iteratively corrected for. The energy conservation error ε of a converged model typically is $< 1\%$.

The process described in this section is schematically shown in figure 9.

3.5 Overview of the input parameters

To summarise, the most relevant input parameters which characterise the model are:

1. The general stellar parameters

   T_{eff} : effective temperature
   R_* : stellar radius
   $\log g$: logarithm of the gravitational acceleration at R_*
   Z : chemical composition[12]

2. the wind structure parameters

   $\dot{M}$: mass loss rate
   v_∞ : terminal wind velocity
   β : wind velocity field parameter

3. and the wind sampling parameters:

   N : number of concentric layers in the model
   l_* : bottom layer of the dynamic region
   R_{max} : maximum outer radius
   p_{min} : percentage of the terminal velocity to set R_{min}
   C : wind sampling cosh-function tuning parameter

`PHOENIX` offers numerous other parameters (see the `PHOENIX` manual [Hau04], but unless mentioned otherwise, the default values have been used and their purposes are not discussed in the scope of this work.

In addition to these three types of modelling parameters there is the input temperature structure the wind structure construction is started from.

[12] Z represents the abundance of all elements except H and He on a logarithmic scale. A metal abundance of $Z = -2$ means fraction of 1/100 of the solar abundances.

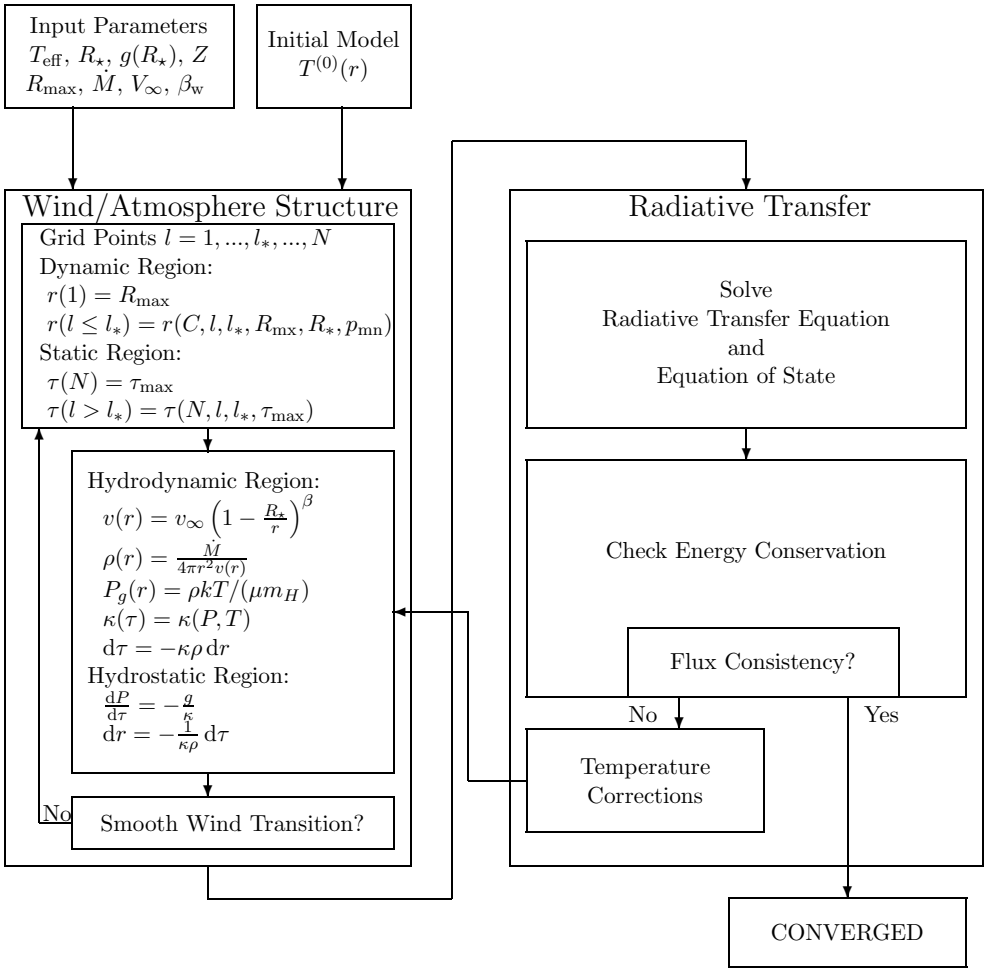

Figure 9: This Flowchart outlines the wind model scheme. A new atmospheric structure is set up (left box) based on an initial input temperature structure. This is repeated until a smooth transition is realised for the at the dynamic/static interface. The new structure is then sent to the general radiation transfer code described in section 3.1. The structure is refined via a temperature correction, until energy conservation is satisfied with enough precision. Then the model is considered converged. (After [Auf00])

Either the output structure of a similar previously calculated model, or, if non available, a comparable non-stellar-wind structure is used. The final model results are independent of the initial temperature structure because of the iterative adjustments made to the structure in order to fulfill the convergence condition (see section 3.4).

4 From hot-wind to cool-wind model

The first step in the modelling process, is to find the limitations of the original hot-wind model when it is applied to cool winds. A convenient way to achieve this is to perform a grid calculation. Model calculations are done for a number of varied parameters, repeatedly varying one of these while keeping all others constant.

After the limitations of the original model are addressed the modifications are described that have been made in the scope of this work, in order to extend the applicability of the wind model to cool winds.

4.1 Determination of the original model limitations

The most interesting model parameters are those that change when moving from hot (super)giants to cool (super)giants. A few selected parameters and corresponding realistic parameter ranges are shown in table 1.

The upper three parameters $T_{\rm eff}$, $\log g$ and the metallicity Z are very general stellar parameters. Except for the effective temperature these are kept constant for all of the models presented in this work with the following values:

the surface gravity $\log g = 0.5$
the metallicity $Z = 0$

The effective temperature is naturally a free parameter, because it is by far the most important stellar atmosphere parameter. It has the largest impact on the shape of a spectrum.

The results of the grid calculation with the original model are shown in figure 10. The first tree columns show the model parameters that are varied

Parameter	Units	typical		min	max	step
		M-K SG	O-B SG	M-K SG		
$T_{\rm eff}$	K	$4,000$	$40,000$	2800	4400	400
$\log g$	cm/s^2	.5	3.0	0	2.0	
Z	$Z_\odot$	0	0	-1	1	
$\log \dot{M}$	$M_\odot$/yr	-7	-7	-10	-5	1
v_∞	km/s	60	1200	10	120	10
β		3.0	3.0	2.5	4.0	

Table 1: The most important parameters influencing wind models, from the top down: effective temperature, gravitational acceleration, metalicity, terminal wind velocity and β. Typical values are given for cool and hot Super-Giants. The parameter ranges represent realistic values for K and M supergiants. Where no step width is specified, the parameter has not been varied for wind models. Instead the typical values have been used.

Teff	VWind	dM/dt	ModID	SpecID	Exit Status	RunTimeM	RunTimeS	ErrMsg
2800	120	E−11	94313	94314	×	00:00:09	00:00:12	interp: logpg out of range
2800	120	E−10	94315	94316	×	00:00:09	00:00:12	interp: logpg out of range
2800	120	E−08	94317	94318	O O	03:43:21	05:07:28	
2800	120	E−06	94319	94320	O O	02:50:17	11:38:08	
2800	60	E−11	94321	94322	×	00:00:24	00:00:04	interp: logpg out of range
2800	60	E−10	94323	94324	×	00:50:22	00:00:05	interp: logpg out of range
2800	60	E−08	94325	94326	×	00:30:04	00:00:06	spultc: temperature .le. 0.d0!
2800	60	E−06	94327	94328	O O	02:47:57	08:18:21	
2800	10	E−11	94329	94330	×	00:17:31	00:00:04	interp: logpg out of range
2800	10	E−10	94331	94473	O O	03:34:43	10:03:30	
2800	10	E−08	94333	94334	O O	03:32:57	07:40:42	
2800	10	E−06	94335	94336	×	00:17:08	00:00:06	accit: not converged to prescribed accuracy!
3200	120	E−11	94337	94338	×	00:00:08	00:00:04	interp: logpg out of range
3200	120	E−10	94339	94340	×	00:20:32	00:00:04	spultc: temperature .le. 0.d0!
3200	120	E−08	94341	94474	O O	01:32:33	05:48:17	
3200	120	E−06	94343	94344	×	00:07:48	00:00:05	accit: not converged to prescribed accuracy!
3200	60	E−11	94345	94346	×	00:00:08	00:00:05	interp: logpg out of range
3200	60	E−10	94347	94348	×	00:18:59	00:00:04	spultc: temperature .le. 0.d0!
3200	60	E−08	94349	94475	O O	01:18:49	05:46:50	
3200	60	E−06	94351	94352	×	00:05:36	00:00:04	accit: not converged to prescribed accuracy!
3200	10	E−11	94353	94354	×	00:20:46	00:00:13	spultc: temperature .le. 0.d0!
3200	10	E−10	94355	94356	O O	02:12:39	06:11:09	
3200	10	E−08	94357	94476	O O	00:49:10	07:46:15	
3200	10	E−06	94359	94360	×	00:45:53	00:00:09	accit: not converged to prescribed accuracy!
3600	120	E−11	94361	94362	×	00:00:08	00:00:05	interp: logpg out of range
3600	120	E−10	94363	94364	×	00:00:17	00:00:04	interp: theta/lg(T) out of range
3600	120	E−08	94365	94366	×	00:00:56	00:00:04	phoenix: wind rgrid problem, stopping.
3600	120	E−06	94367	94477	O O	00:34:39	06:05:23	
3600	60	E−11	94370	94371	×	00:00:32	00:00:05	interp: logpg out of range
3600	60	E−10	94372	94373	×	00:00:31	00:00:05	fcthyd: convection theta .lt. 0!
3600	60	E−08	94374	94375	×	00:00:39	00:00:04	phoenix: wind rgrid problem, stopping.
3600	60	E−06	94376	94377	O O	00:40:24	06:27:21	
3600	10	E−11	94378	94379	×	00:00:16	00:00:04	interp: theta/lg(T) out of range
3600	10	E−10	94380	94381	×	00:00:16	00:00:05	fcthyd: convection theta .lt. 0!
3600	10	E−08	94382	94383	O O	00:35:57	01:49:51	
3600	10	E−06	94384	94385	×	00:10:53	00:58:16	accit: not converged to prescribed accuracy!
4000	120	E−11	94386	94387	×	00:00:35	00:00:04	interp: logpg out of range
4000	120	E−10	94388	94389	×	00:00:42	00:00:04	phoenix: wind rgrid problem, stopping.
4000	120	E−08	94390	94391	×	00:00:43	00:00:04	phoenix: wind rgrid problem, stopping.
4000	120	E−06	94392	94393	O O	00:40:02	01:19:47	
4000	60	E−11	94394	94395	×	00:00:09	00:00:05	interp: logpg out of range
4000	60	E−10	94396	94397	×	00:00:34	00:00:05	gradad: ierr .ne. 0, matrix singular
4000	60	E−08	94398	94399	×	00:00:18	00:00:04	fcthyd: convection theta .lt. 0!
4000	60	E−06	94400	94401	O O	00:35:40	05:47:57	
4000	10	E−11	94402	94403	×	00:00:34	00:00:18	gradad: ierr .ne. 0, matrix singular
4000	10	E−10	94404	94405	×	00:00:25	00:00:09	fcthyd: convection theta .lt. 0!
4000	10	E−08	94406	94407	O O	00:35:50	01:32:40	
4000	10	E−06	94408	94409	×	00:15:13	06:39:36	accit: not converged to prescribed accuracy!
4400	120	E−11	94410	94411	×	00:00:09	00:00:08	interp: logpg out of range
4400	120	E−10	94412	94413	×	00:00:12	00:00:06	fcthyd: pgas < 0!
4400	120	E−08	94414	94415	×	00:00:12	00:00:07	fcthyd: pgas < 0!
4400	120	E−06	94416	94417	×	00:00:10	00:00:08	fcthyd: pgas < 0!
4400	60	E−11	94418	94419	×	00:00:08	00:00:07	interp: logpg out of range
4400	60	E−10	94420	94421	×	00:00:11	00:00:07	fcthyd: pgas < 0!
4400	60	E−08	94422	94423	×	00:00:13	00:00:08	fcthyd: pgas < 0!
4400	60	E−06	94424	94425	×	00:00:12	00:00:07	fcthyd: pgas < 0!
4400	10	E−11	94426	94427	×	00:00:13	00:00:09	fcthyd: pgas < 0!
4400	10	E−10	94428	94429	×	00:00:12	00:00:04	fcthyd: pgas < 0!
4400	10	E−08	94430	94431	×	00:00:35	00:00:04	fcthyd: pgas < 0!
4400	10	E−06	94432	94478	O ×	00:42:37	15:11:24	=>> PBS: job killed: walltime 54008 exceeded limit

Figure 10: Results from a grid calculation with the original model performed in order to find the limitations of the hot-wind model when it is applied to cool winds. This is the output of a batch program constructed to manage the grid calculations performed in the scope of this work. Only 15 out of 60 models did not terminate prematurely. The `Teff` $= T_{\rm eff}$, `VWind` $= v_\infty$ and `dM/dt` $= \dot{M}$ are in the units K, km/s and $M_\odot$/yr respectively.

in the grid. The 4th and 5th column show the Process IDs belonging to the calculations of the model and the corresponding spectrum respectively. The 6th (double) column shows the exit status of the model/spectrum calculations. The 7th and 8th column gives the calculation time. The last column the error message the calculation exits with when not successful. Only 15 out of 60 models finished the specified number of iterations, 20 in this case. However, just finishing the 20 iterations does not imply that the model converged.

There are nine different error messages shown in the last column of figure 10. Not all of them are caused by errors in the atmospheric structure. For example the error for the model with $\{T_{\rm eff}, v_\infty, \dot{M}\} = \{4400, 10, 10^{-6}\}$ in the units of table 1 on page 40

```
=>> PBS: job killed:  walltime 54008 exceeded limit
```

comes from the job queuing system that killed the computation because it took longer than the time reserved for it, 15 hours in this case. It is likely however, that the spectrum calculation would have been completed successfully in a bit more time. The spectrum computation is in fact just one more iteration[13], of which just 20 passed before. Besides, there are other spectrum computations that took almost 12 hours to complete ($\{T_{\rm eff}, v_\infty, \dot{M}\} = \{2800, 120, 10^{-6}\}$ in the usual units) whereas others only need 1 hour and 30 minutes ($\{T_{\rm eff}, v_\infty, \dot{M}\} = \{4000, 10, 10^{-8}\}$ in the usual units).

Nevertheless, there are a lot of errors that are caused by improper construction of the atmosphere. Some of these can be resolved by individual fine tuning. But except from the fact that it is very laborious, a principally better method is to adapt the atmosphere construction originally intended for hot stellar winds to cold-wind modelling.

4.2 Unaltered basic assumptions

Although cool winds are principally completely different from hot winds (see section 2.2), the most fundamental assumptions made for the hot-wind model can be kept unchanged:

1. time independent, steady state
2. radial symmetry
3. β velocity law
4. smooth single-phase flow, so no dust
5. no mechanical dissipation, heat conduction or viscosity
6. no magnetic fields

[13]The fundamental difference, is that after every iteration in the wavelength loop the radiation field is Lorentz transformed from the comoving Lagrange frame into the Euler frame. This difference, however, is not relevant for the convergence of the model.

7. no rotation effects
8. constant chemical abundances throughout the (extended) atmosphere

The things that do change are described in the following.

4.3 Upper boundary

4.3.1 Low pressure problem

Figure 10 shows that non of the models for low mass loss rates of $\dot{M} = 10^{-11}\dot{M}/\mathrm{yr}$ completed successfully. Most of these terminated with the message

```
interp:  logpg out of range!
```

For the calculation of the equation of state (EOS) partial pressure tables are used that have a limited pressure range. The pressures in winds with small $\dot{M}$, are by far smaller than the normal atmospheric ranges.

Therefore, the first step to tackle the low pressure problem is to compute new pressure tables with lower ranges with `csppress` (see the `PHOENIX` manual [Hau04]). The pressure tables have a prescribed format, in which the pressure range extends over 19 orders in predefined steps. The normal range of the gas pressure in the tables is $10^{9} - 10^{-10}\,\mathrm{dyn/cm^2}$, whereas the newly calculated tables have ranges from $10^{8} - 10^{-11}$, $10^{7} - 10^{-12}$, $10^{6} - 10^{-13}$ and $10^{5} - 10^{-14}\,\mathrm{dyn/cm^2}$. It turned out that in the last two tables the upper pressure limit is too low for the inner shells of the hydrostatic parts of the atmosphere. In practice the table with the range $10^{7} - 10^{-12}\,\mathrm{dyn/cm^2}$ proved to be the most useful.

The new limit of the gas pressure

$$P_g \not< 10^{-12} \quad \mathrm{dyn/cm^2} \tag{73}$$

is a factor 100 smaller, but in many cases still not small enough. The next step is that regions with a pressure of less than $10^{-12}\,\mathrm{dyn/cm^2}$ are so optically thin, that their contribution to the spectrum can easily be neglected. This means, that the extent of the radial grid must be reduced until the outer layer is within the range of the table. The scheme used for this stripping off of outer layers is:

1. construct the radial grid $r(l)$
2. compute the state of the top layer $r(1)$
3. check whether $P_g(1) > 10^{-12}$
4. if not, reduce the radial range according to

$$R_{\max} = R_{\max} \cdot \left[1 - 0.2\left(3 - 2\frac{P_g(1)}{10^{-12}}\right)\right] \tag{74}$$

in which the factors 0.2, 3 and 2 are chosen in such a way that the range is reduced between 20% in case that the outer pressure is close to the target value and 60% if it is still way off.

These steps are repeated until the condition of step 3 is met. This iteration is very fast because only one layer needs to be computed.

When hot winds are modelled, the wind temperatures are high enough that molecules do not need to be considered in the equation of state. This significantly reduces the calculation time, so that the equation of state can be calculated from scratch for every model again. Therefore, the low outer pressure problem does not occur for hot-wind models. Nevertheless, it is useful to strip off the layers with extremely low pressures. These layers have a negligible effect on the spectrum and can rather be used for the wind regions where the influences on the spectrum are large and change rapidly from layer to layer.

4.3.2 Start new iterations from initial values

In the iterative process described above another problem emerges. When the state of the top layer is computed, the environmental variables $T(1)$, $P_g(1)$ and $g(1)$ are recalculated and the old values are overwritten. The calculation is not very precise at this stage and is meant as a initial guess needed to successively perform the full precise LTE calculation. But when the unprecise values are repeatedly reused, the initial deviations are repeatedly amplified. The errors can become so large that the subsequent structure calculations yield invalid structures (e.g. negative temperatures). This problem of progressive error amplification is solved by making an initial backup of the three parameters that are altered in the top layer setup and restored before every following top layer calculation. In addition the initial $R_{\max}$ is stored as the reference radius of the restored values. Thus every new calculation starts from scratch.

4.3.3 Inexact reassignment

The modifications that finally solved the outer low pressure issue mainly affected the top layer setup. But another problem, occasionally affecting model or spectrum calculations for which a preceding model was unaffected, has been found to originate from the top layer setup

```
s3init:  beta inversion!
```

caused by a non-monotonic velocity field. The layer in which the velocity in those cases is not monotonic appeared to be the outer layer. The wind velocity for large r becomes almost constant (but still increases), and the decrease in the last layer is not very obvious as it occurs typically after the

15th decimal place. This is due to a wrong reassignment of the outer velocity

$$v(1) = \frac{\dot{M}}{4\pi r(1)^2 \rho_{\text{out}}} \tag{75}$$

in which ρ_{out} is a common block variable in `PHOENIX` that is not in all cases exactly equal to $\rho(1)$, which is defined in Eq. (57) in the top layer setup. The problem has been solved by removing the reassignment, which is equivalent to exchanging ρ_{out} by $\rho(1)$ in Eq. (75) for an exact reassignment.

4.4 Lower boundary

4.4.1 Thin hydrostatic region problem

Another problem arises in the static part of the atmosphere. The static part is sampled quite roughly with typically only 15 layers to save layers for the dynamic part. In the static layers setup first an optical depth grid $\tau(l)$ is constructed, based on the bottom value of the wind region $\tau(l_*)$ (see page 35). The slope of this grid increases with decreasing number of static layers and with decreasing optical depth at the interface $\tau(l_*)$. The slope of the τ-grid is not allowed to be too large because large steps in τ are problematic when solving the radiation transport equation (section 3.1.4). To prevent the slope from becoming to large, a maximum slope was hardcoded into the model overruling the target maximum value $\tau_{\max}$.

The optical depth of the interface depends on the mass loss rate via the density. The lower mass loss rate models here give rise to a problem. The largest value that is reached for τ for low mass loss rates (i.e., $\dot{M} \lessapprox 10^{-9}$) is typically one or two orders lower than $\tau_{\max}$. Thus the complete atmosphere is thin at the wavelength λ_{std} at which the τ-grid was constructed.

The solution to this problem is obvious: the hardcoded maximum slope must be replaced by a method that reduces the needed slope to such extent that the hardcoded maximum isn't even reached. In order to lower the needed slope first the number of static layers $N - l_*$ is increased. This aim can be merged into the corrections of section 4.3 where the outer layers are stripped off by reducing $R_{\max}$. There the stripped shells were all released to the wind region, where they had been taken from, so that the parameter l_* was left unchanged. Now they will be equally divided between the wind region and the static region. To the sequence on page 43 another step is added:

5. release the outer shell alternatingly to the static or wind region

$$l_* = l_* - \delta_{\text{top}} \qquad \text{with} \quad \delta_{\text{top}} = 0, 1 \tag{76}$$

where δ_{top} is toggled between 0 and 1 every iteration starting with 1.

Although at the top layer setup procedure nothing is known about a possible problem at the bottom, it is justified to release shells to the static region, because if the wind is too optically thin at the top, then it will be relatively thin at the transition layer either. Therefore, the extra layers for the hydrostatic region will be needed there after the top layer setup anyway.

But in spite of this modification to the top layer setup the required slope is not always achieved. The outer layers of the wind in these cases are often optically very thin, with values of $\tau \lessapprox 10^{-10}$ and maybe a few more can be stripped off here. This optical depth is based on continuum processes only, and only for one wavelength. The line extinction coefficients can be up to 8 orders larger than the continuum coefficients. In order to make sure that the optical depth of the outer shell with the contributions of line processes included does not fall below 10^{-1} at all wavelengths for the strongest lines, only the layers for which $\tau(l) < 10^{-10}$ are released additionally. Again these are equally divided (approximately) between the wind and the static region

$$l_* = l_* - \delta_{\rm bot} \qquad \text{with} \quad \delta_{\rm bot} = \text{floor}(\text{N}_{\rm now}/2) \tag{77}$$

where $N_{\rm now}$ represents the number of no-wind ($\tau(l) < 10^{-10}$) layers.

But still, the extra layers now available to the static region reduce the slope not always enough to get below the maximum. The second way to decrease the slope is to increase the optical depth at the interface $\tau(l_*)$. This is done by reducing $R_{\rm min}$. The velocity law approaches 0 when $r \to R_*$. It follows from Eq. (57) that ρ approaches ∞ when $r \to R_*$. By moving closer to the star the density and thus the optical depth at the transition interface can be increased.

The initial value of $R_{\rm min}$ is determined in the original model with the parameter $p_{\rm min}$, with a default value of $p_{\rm min} = 0.002$. If the first two attempts to decrease the slope of the τ-grid described above have not been sufficient, the minimal velocity of the wind region is iteratively reduced according to

$$p_{\rm min} = p_{\rm min}/10 \tag{78}$$

until the condition

$$\tau(l_*) \leq \tau_{\rm max}/10^{d_{\rm max}(N-l_*)} = 10^{2-0.3(N-l_*)} \tag{79}$$

is met, where $d_{\rm max} = 0.3$ is the hardcoded maximum slope. Every time a new value for $p_{\rm min}$ is set, a new radial grid is made and the wind region structure is recomputed down to the bottom in order to check condition (79).

4.4.2 Radial grid fix

The three modifications described above effect that thin hydrostatic regions no longer occur. However, while examining the radial structure being modified by the loop described above, a problem has been found that causes

the outer radius to change unintentionally every time the radial grid is recomputed. The radial grid as described by equation (59) does not generally satisfy $r(1) = R_{\max}$. Although the deviations are not very large, i.e. in the order of a few percent, the many recomputations performed in the modified model make the deviation grow increasingly. The corrected expression for the radial grid setup is

$$r(l) = R_{\min} + \{R_{\max} - R_{\min}\}\frac{\cosh\left(C\frac{l_*-l}{l_*-1}\right) - 1}{\cosh(C) - 1} \tag{80}$$

which satisfies both $r(1) = R_{\max}$ and $r(l_*) = R_{\min}$.

4.5 Transition boundary

4.5.1 Improve smoothing process

The smoothing process as it is implemented in the original wind model (see section 3.3.3) does not work as desired in many cool-wind cases. In figure 10 the four models with the message

```
phoenix:  wind rgrid problem, stopping.
```

aborted due to insufficient smoothing. This problem is not as rare as the list suggests with only four out of sixty models. The other frequent errors that occur in the list are due to the upper and lower boundary problems that are described above. The structure check is the last step of the grid setup iteration. So only models which survive the earlier steps are prone to this problem.

In the smoothing procedure (see section 3.3.3), the density is checked at the hydrodynamic-static transition Δ_B and at the transition directly above it Δ_A. Δ_B is decreased by moving l_* towards $l_* + 1$ using the target density ρ'_*. Δ_A is decreased by moving the points in the bottom of the wind region $l < l_*$ closer together (so towards l_* because l_* is fixed) by increasing the radial sampling constant C. The effect of increasing C is shown in figure 12.

The jump that causes the "r-grid problem" in most cases is Δ_A. If the threshold $\Delta_A > 5$ is exceeded, the original model not only increases C but also uses the new target density ρ'_* of Eq. (68) to set $R_{\min}$. The new $R_{\min}$ improves Δ_B a bit but at the same time makes Δ_A much worse. When setting the new $R_{\min}$ via the target density l_* moves faster up towards $l_* + 1$ than $l_* - 1$ to l_* because of the increasing slope when moving towards the star (see figure 11). The little increase of $C = C + 1/10$ in the original model in most cases can not compensate for this effect, not to speak of improve the jump.

The smoothing procedure performs much better when the new target density is prevented to be set in case that Δ_A is too large. However, the Δ_A

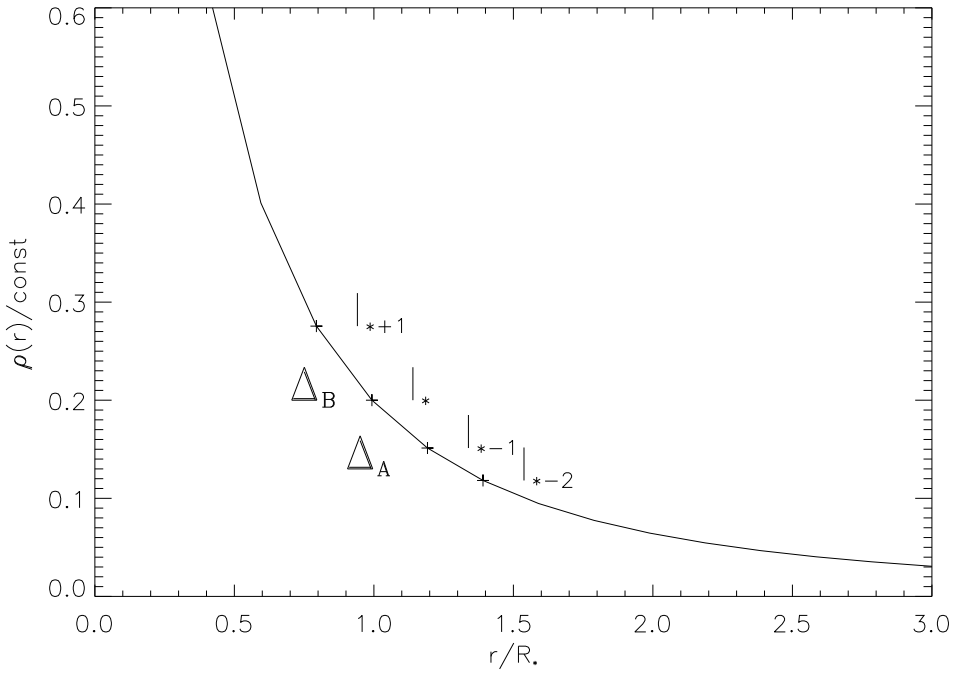

Figure 11: An artificial density curve with four sampling points belonging to the layers $l_* - 2$, $l_* - 1$, l_* and $l_* + 1$. The density jumps $\Delta_{\rm A}$ and $\Delta_{\rm B}$ are between the layers $l_* - 1$ and l_* and the layers l_* and $l_* + 1$ respectively.

problem still is not completely solved, which means that the C correction of Eq. (71) is insufficient with the built in limit of 10 iterations, so that the bottom layers of the wind region are still too far apart (see figure 11).

The influence of C on the radial grid is shown in figure 12. If the original model is started with the default value of $C = 5.0$ it can increase to $C = 5.0 + 10 * 0.1 = 6.0$ at most (see section 3.3.3). In order to both extend the range of the parameter C and reduce the number of iterations required for smoothing, the step width of C is increased by a factor of 5. The new correction to the jump Δ_A is

$$C = C + 5/10 \tag{81}$$

for every iteration.

With these modifications, the smoothing problems no longer occur.

4.5.2 Avoid remappings of a mismapped temperature structure

The basic idea behind the construction of the atmosphere (see section 3.3) is to start with an initial guess for a radial grid (parameters $p_{\rm min}$, $R_{\rm max}$ and C). Then an atmosphere is constructed based on the guess in which one step is to map the temperature structure on the initial grid. Subsequently, the

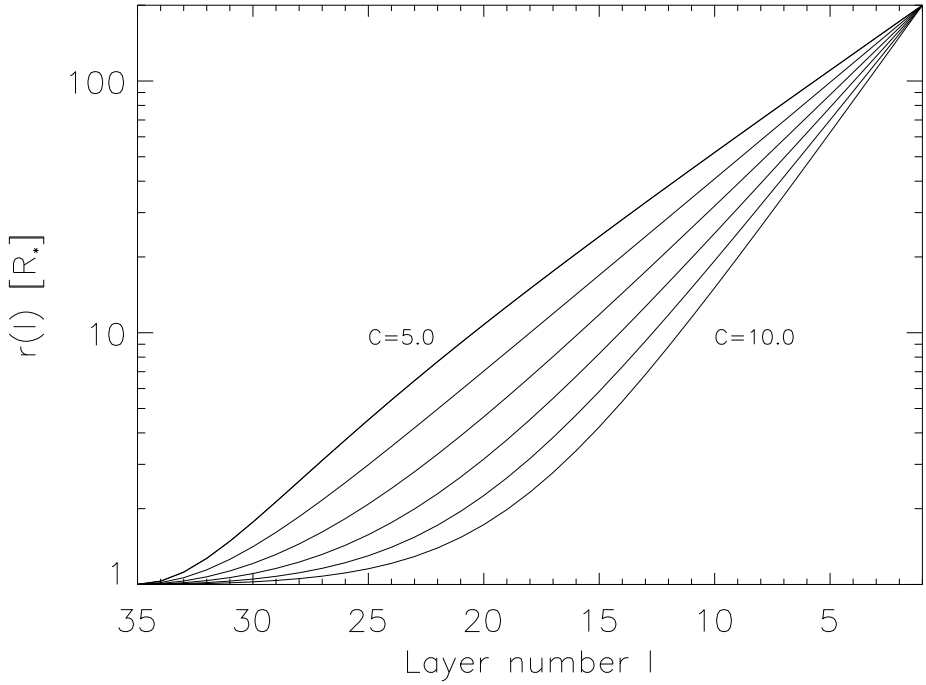

Figure 12: Six radial sampling curves for values of the parameter C from $C = 5.0$ to $C = 10.0$ with a stepsize of 1.0. The radii are given in units of the stellar radius R_* whith a maximum radius of $R_{\max} = 200R_*$. On the x-axis the layer numbers are shown with a typical total of 35 for the wind region. Increasing C lowers the slope of the lower layers (closer to the star, with higher layer number) and steepens the slope in the outer regions of the wind.

initial parameters are refined. This scheme is iterated until the constructed atmosphere satisfies the specified conditions.

When the τ grid that is constructed during the first iteration deviates much from the final grid, the interpolations made during the atmosphere construction process can yield a very unusable temperature structure. Consequent remappings of this initial mismapping in the best case leads to a non-optimal atmosphere, but more frequently the calculation stops after some iterations.

The basic idea of an initial guess that is iteratively refined has been extended in many of the modifications made for cool winds. Therefore, an important last modification to the hot-wind model is to save the initial temperature structure $T^{(0)}(\tau)$ and reuse the saved structure instead of the remapped structure for next iterations where the parameters $p_{\min}$, $R_{\max}$ and C are refined. This is in complete analogy to the modification described in 4.3.2 where the top layer is saved and restored for the same purpose.

5 The first results with the new model

With the modifications made to the original model described in chapter 4 it is now interesting to see how the modified model performs when atmospheres of cool-wind stars are calculated. In the first place the ability is tested to setup atmospheric structures that are able to converge. In addition, the spectra produced by the model calculations are examined to contain characteristic wind features, like those used for observing cool stellar winds described in chapter 2.4

In this section the bare results are shown for these two tests. A discussion of the results is found in section 6.

5.1 Model grid recalculated with the modified code

The grid calculation that was performed with the original model (see figure 10) has been repeated with the modified model. The model parameters have not been changed in order to give a fair comparison between the old and the new grid results (except for the three grid parameters: effective temperature, terminal wind velocity and mass loss rate). The new results are shown in figure 13.

Not all models have finished successfully. One type of error has occurred for two models. This type of error is due to an unsuitable value of a general `PHOENIX` parameter, `taulin`. The effect of `taulin` on the wind model calculations is described in section 6.1. When the `taulin` value is increased a little bit (from 10^{-3} to 10^{-2}) *all models finish successfully.*

The grid had originally been calculated to find the limitations of the hot-wind model when it is applied to cool winds. The limitations of the original model are thus found to be resolved with the modified model.

Teff	VWind	dM/dt	ModID	SpecID	Exit Status	RunTimeM	RunTimeS	ErrMsg
2800	120	E-110	93823	93989	O O	03:53:21	06:01:51	
2800	120	E-100	93824	94111	O O	07:34:14	04:22:39	
2800	120	E-080	93825	93990	O O	04:57:14	07:50:02	
2800	120	E-060	93826	94136	O O	07:24:16	13:54:04	
2800	060	E-110	93918	94018	O O	04:23:07	06:01:21	
2800	060	E-100	93919	94022	O O	04:18:15	04:26:26	
2800	060	E-080	93920	94046	O O	05:21:41	06:53:59	
2800	060	E-060	93921	94045	O O	07:42:08	11:20:45	
2800	010	E-110	93833	93992	O O	04:57:23	06:12:13	
2800	010	E-100	93834	94140	O O	05:18:47	05:50:28	
2800	010	E-080	93835	94141	O O	03:26:37	08:40:17	
2800	010	E-060	94024	94117	x x	00:51:51	00:15:38	accit: not converged to prescribed accuracy!
3200	120	E-110	94026	94128	O O	04:42:05	03:11:30	
3200	120	E-100	94027	94129	O O	05:13:38	02:46:46	
3200	120	E-080	94028	94137	O O	03:09:15	02:08:54	
3200	120	E-060	94029	94119	O O	00:37:11	01:27:00	
3200	060	E-110	94031	94138	O O	04:23:45	01:29:28	
3200	060	E-100	94032	94144	O O	02:39:20	01:23:17	
3200	060	E-080	94033	94150	O O	03:25:16	02:30:54	
3200	060	E-060	94034	94435	O O	00:38:51	00:29:25	
3200	010	E-110	94036	94312	O O	03:48:40	01:23:42	
3200	010	E-100	94453	94653	O O	03:32:05	03:34:53	
3200	010	E-080	94038	94145	O O	00:42:26	03:56:36	
3200	010	E-060	94039	94146	x x	00:08:13	00:10:51	accit: not converged to prescribed accuracy!
3600	120	E-110	94041	94151	O O	00:41:33	01:43:35	
3600	120	E-100	94042	94152	O O	00:41:33	01:02:55	
3600	120	E-080	93941	94023	O O	00:41:10	01:14:59	
3600	120	E-060	93942	94043	O O	00:39:03	08:15:02	
3600	060	E-110	93944	94047	O O	00:41:29	01:11:31	
3600	060	E-100	93945	94054	O O	01:13:57	01:30:32	
3600	060	E-080	93946	94048	O O	00:41:29	01:13:07	
3600	060	E-060	93947	94049	O O	00:40:01	08:26:03	
3600	010	E-110	93949	94058	O O	01:12:17	01:24:12	
3600	010	E-100	93950	94059	O O	01:02:30	01:31:24	
3600	010	E-080	94135	94368	O O	00:41:41	01:04:36	
3600	010	E-060	93952	94056	O O	00:38:32	06:59:22	
4000	120	E-110	93954	94065	O O	00:41:13	01:25:59	
4000	120	E-100	93955	94081	O O	00:41:17	01:27:43	
4000	120	E-080	93956	94082	O O	00:41:25	01:23:14	
4000	120	E-060	93957	94083	O O	00:39:10	05:49:08	
4000	060	E-110	93959	94085	O O	00:41:54	01:36:25	
4000	060	E-100	93960	94086	O O	00:54:47	01:10:48	
4000	060	E-080	93961	94087	O O	00:41:39	01:11:42	
4000	060	E-060	93962	94088	O O	00:39:51	11:37:35	
4000	010	E-110	93964	94090	O O	00:41:26	01:27:36	
4000	010	E-100	93965	94091	O O	00:43:16	01:15:07	
4000	010	E-080	93966	94092	O O	00:42:09	01:30:16	
4000	010	E-060	93967	94094	O O	00:40:58	11:02:58	
4400	120	E-110	93969	94096	O O	00:41:40	01:05:05	
4400	120	E-100	93970	94095	O O	00:41:32	00:58:37	
4400	120	E-080	93971	94097	O O	00:42:00	01:07:19	
4400	120	E-060	93972	94098	O O	00:39:32	02:59:01	
4400	060	E-110	93974	94100	O O	00:37:09	01:07:26	
4400	060	E-100	93975	94101	O O	00:45:15	00:50:05	
4400	060	E-080	93976	94103	O O	00:42:16	01:24:12	
4400	060	E-060	93977	94102	O O	00:39:48	12:29:10	
4400	010	E-110	93979	94105	O O	00:41:19	01:06:48	
4400	010	E-100	93980	94107	O O	00:42:18	00:52:36	
4400	010	E-080	93981	94108	O O	00:43:13	00:55:55	
4400	010	E-060	93982	94106	O O	00:36:47	13:07:15	

Figure 13: Results from a grid calculation with the modified model. This is the output of a batch program constructed to manage the grid calculations performed in the scope of this work. Only 2 out of 60 models terminated prematurely. This grid has been calculated with exactly the same settings as the grid shown in figure 10 on page 41, but now the modified wind model has been used instead of the original hot-wind model. The two models that did not converge in this grid converge when increasing `taulin` (a general `PHOENIX` parameter, see section 6.1) a bit.
Here the uncorrected table is shown for a fair comparison with figure 10, for which no fine tuning has been done either.

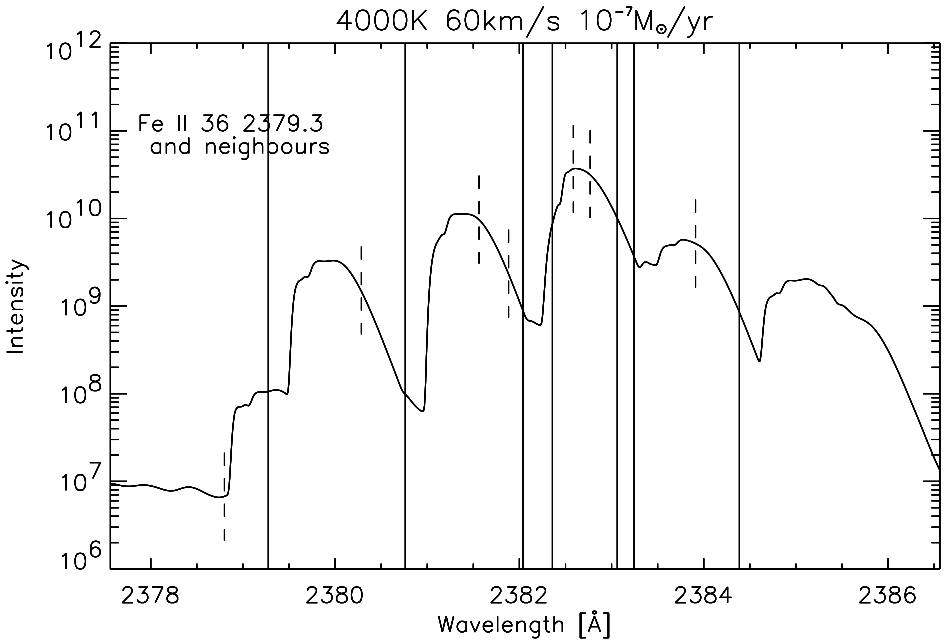

Figure 14: Many UV emission lines in cool-wind spectra are found to be close together so that their profiles overlap. The lines shown here are all Fe II lines. The vertical lines mark the line centers, the little dashed lines indicate the doppler shift $\Delta\lambda = -\lambda_0 v_\infty/c$ for the outermost model layers where the terminal velocity is reached. The profile of the Fe II 36 2379.8Å line that is also found in figure 3 can not be discerned.

5.2 Characteristic UV emission lines

UV emission lines contain important observational characteristics of cool stellar winds (see section 2.4). Many of the observational emission lines shown the figures 3 and 4 are found in the spectra calculated with the wind model. However, some of them are found to be partially overlapped by neighbouring lines. The overlap increases when v_∞ is increased because the lines then broaden. An example is given in figure 14, where the Fe II 36 2379.3Å line (one of the lines of figure 3) is shown with its close neighbours.

Overlapping lines first have to be disentangled to obtain the profiles of the individual lines. This is beyond the scope of this work. Since here is only looked for a qualitative evaluation of UV line profiles, some lines that have no close neighbours are selected. The lines have been picked from the list from Judge [JJ91] that was used for the observed spectral lines of figure 3.

Figure 15 shows four UV line profiles. The two on the left are also found in the observed spectra of figure 3 and 4. The Fe II 1 2625.6Å line profile on the left side flows over to the neighbouring Fe II 1 2621.7Å line. Instead of the Fe II 3 2332.8Å observed line, which has a neighbouring Fe II 35 line

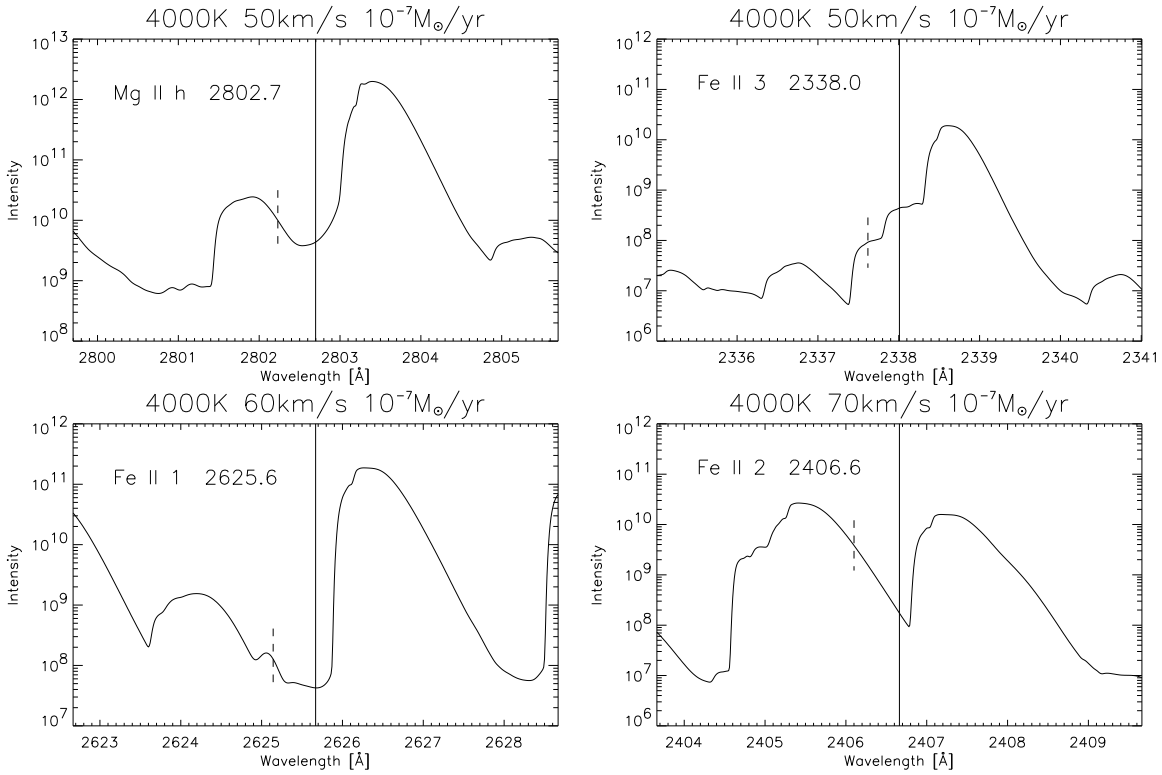

Figure 15: Four UV emission lines with wind absorption cores in synthetic spectra from the modified wind model in `PHOENIX` . The values of the model parameters $T_{\rm eff}$, v_∞ and $\dot{M}$ are given in the plot titles. The vertical lines mark the line centers, the little dashed lines indicate the doppler shift $\Delta\lambda = -\lambda_0 v_\infty/c$ for the outermost model layers.

at 3231.3Å, the Fe II 3 2338.0Å line is plotted here. In addition the Fe II 2 2406.6Å is plotted because of it's typical shape without neighbour effects.

In figures 16 and 17, the same profiles are shown for varied values of v_∞. At the lowest velocity of 10km/s some of the emission lines are not yet present. Then at first the absorption core shifts from the middle towards lower wavelengths. At higher velocities the core can no longer be clearly discerned but an asymmetry is still found.

The synthetic profiles are found to be very similar to the observed profiles shown in figure 3 and 4. The results shown here are obtained without tuning any modelling parameter in order to find a good fit. Apparently `PHOENIX` is very capable of modelling cool stellar wind spectra.

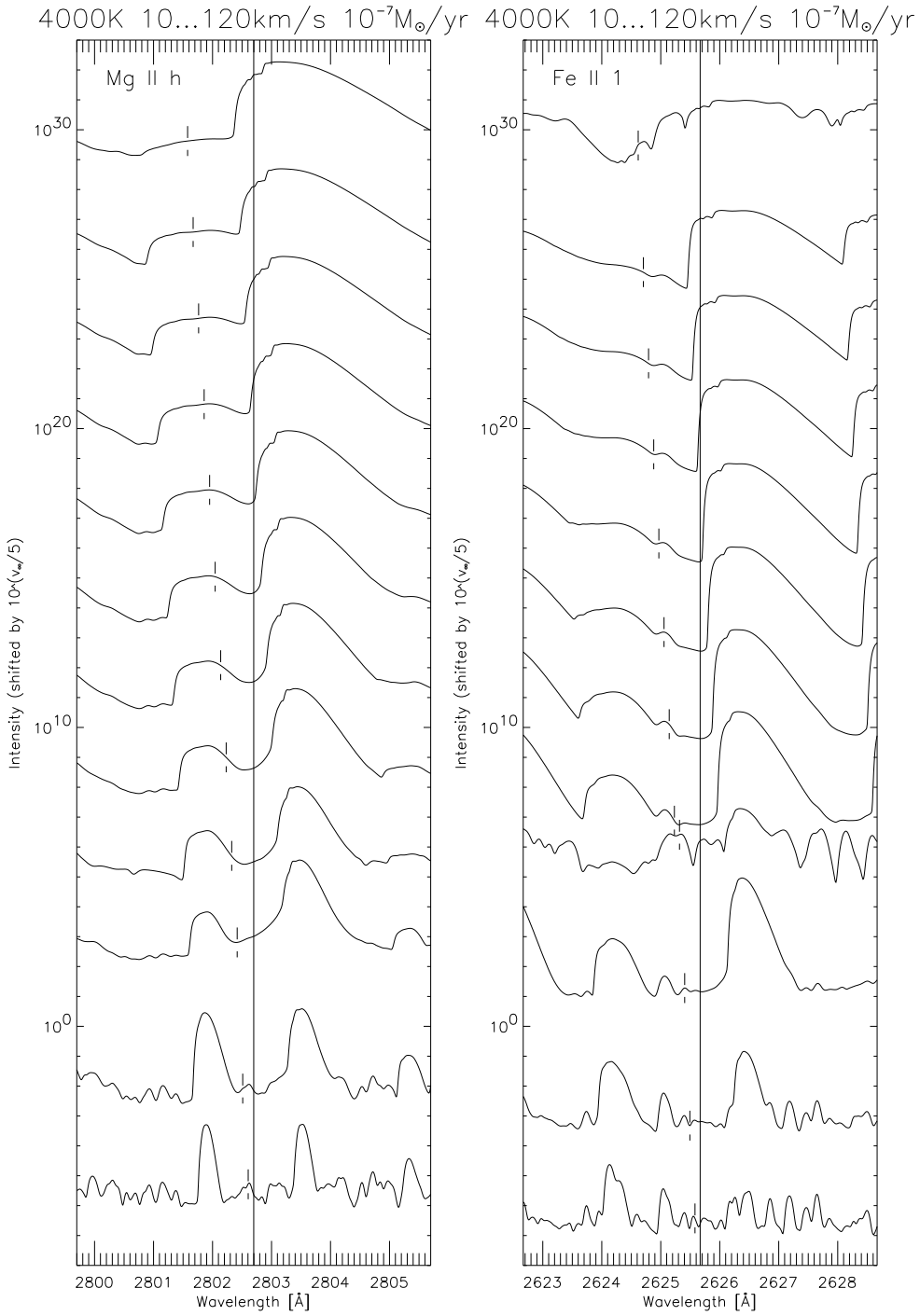

Figure 16: The emission lines Mg II h 2802.7Å and Fe II 1 2625.6Å that are also shown in observed spectra in figure 3 and 4 for different values of the terminal velocity v_∞ ranging from 10km/s for the lowest to 120km/s for the highest curve. The lines are scaled by a factor 100 per 10km/s step. The solid vertical lines mark the line centers, the small dashed ones the doppler shift for v_∞.

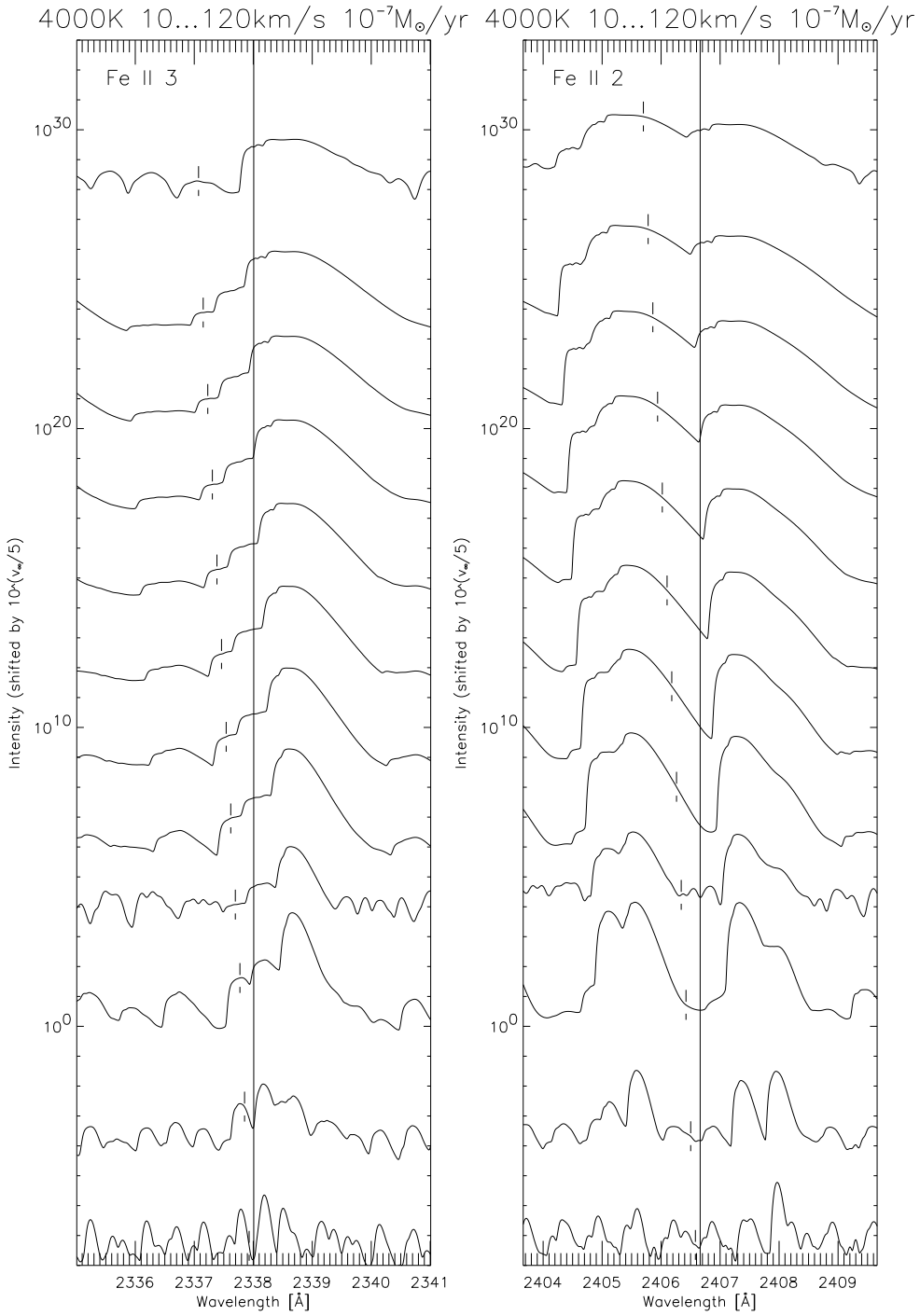

Figure 17: The emission lines Fe II 3 2338.0Å and Fe II 2 2406.6Å of figure 15 for different values of the terminal velocity v_∞ ranging from 10km/s for the lowest to 120km/s for the highest curve. The lines are scaled by a factor 100 per 10km/s step. The solid vertical lines mark the line centers, the small dashed ones the doppler shift for v_∞.

6 Discussion

In the previous chapter was shown that the modified wind model constructs converging cool-wind atmospheres. Furthermore, the resulting synthetic spectra show the characteristic observational cool-wind features. It has also been shown that in certain specific cases even with the modified wind model some tuning is needed for the model to converge (see figure 13). In this section, the reason for this tuning requirement is discussed. Furthermore, a few possible refinements of the modelling process are proposed that should further improve the convergence of the wind model calculations and the accuracy of the obtained wind spectra.

6.1 Further fine tuning

In section 5.1 has been mentioned that models that do not converge with the modified wind model can be tuned with the parameter `taulin`. `taulin` is a general `PHOENIX` parameter (see the `PHOENIX` manual [Hau04]) which influences the way the source function is interpolated on a new τ-grid along a characteristic ray, see equation (50). When the step in the optical depth along a characteristic ray $\Delta\tau^k$ is greater than `taulin`, parabolic interpolation is used instead of linear.

In the outer regions of the wind model the temperature and the source

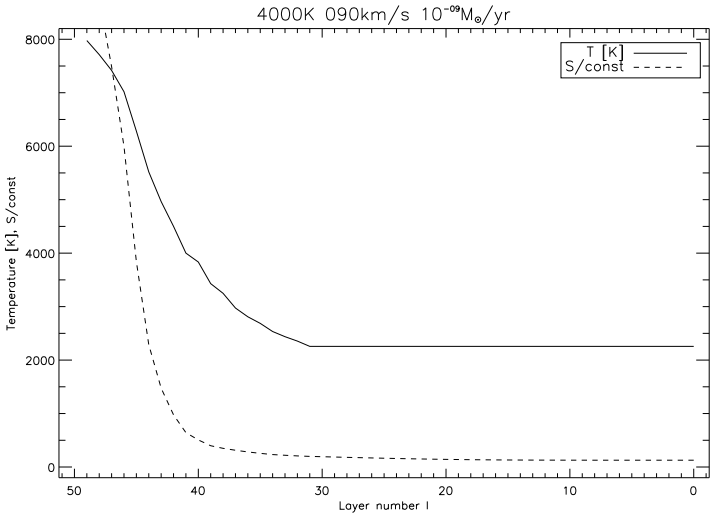

Figure 18: The final temperature and mean intensity (at $\tau = \tau_{\rm std}$) structures of a model with the parameters $\{T_{\rm eff}, v_\infty, \dot{M}\} = \{4000, 90, 10^{-9}\}$ in the usual units. On the x-axis the layer number minus 1 $l-1$ is shown. In the outer region of the wind, from layer 1 to about 30 (0 to 29 in the plot), the temperature is rather constant. This generally is the case for wind models.

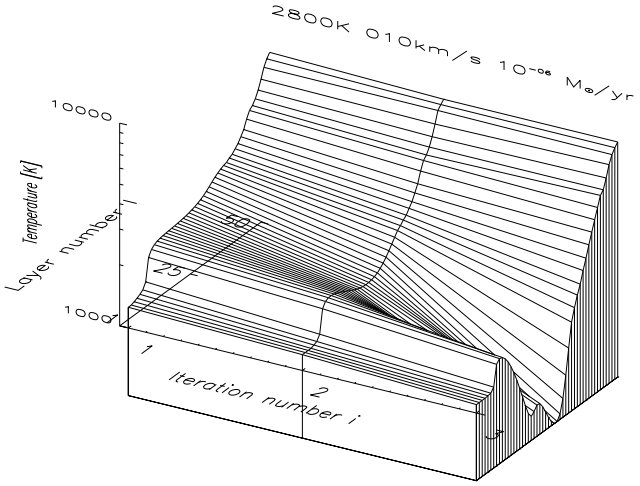

Figure 19: The fatal evolution of a temperature structure when in problematic cases `taulin` is increased too much. The x-axis shows the iteration number i from 1 to 3, the y-axis the layer number l from 1 to 50, the z-axis shows the temperature in K. In a certain iteration a temperature inversion develops. In subsequent iterations this local minimum falls further down, until it gets below 0 K. In the case shown here, this happened after the second iteration.

function typically are rather constant, see figure 18. Interpolating a constant function piecewise with parabolic fits can give a very imprecise result. Besides, these interpolations are not stable, meaning that from iteration to iteration the values oscillate around the constant value. Through the interpolated source function the computed corrections to the mean intensity J in Eq. (45) then are imprecise. The accelerated lambda iteration stops when the prescribed accuracy is not reached after a maximum number of iterations, which is 50 by default. When the computed corrections to J in the last iteration are still not much smaller than in the first, increasing the maximum number of iterations will not help. Tuning `taulin` can give a solution in many cases.

Higher values of `taulin` imply that a linear interpolation is also used in cases where the steps in the optical depth are larger. For a coarsely sampled curve (with large steps in the sampling grid) a linear interpolation gives inaccurate values between two points. So increasing `taulin` increases the inaccuracy of the radiation field computations in Eq. (45), which directly enters the temperature correction in Eq. (53).

When `taulin` is set too high, temperature inversions emerge in the structure. These inversions are amplified in subsequent iterations and the calculation finally stops when the temperature in the minimum falls below 0 K (typically after two or three iterations). The temperature structure evolution for such a case is shown in figure 19.

There is another parameter to tune, the temperature correction attenu-

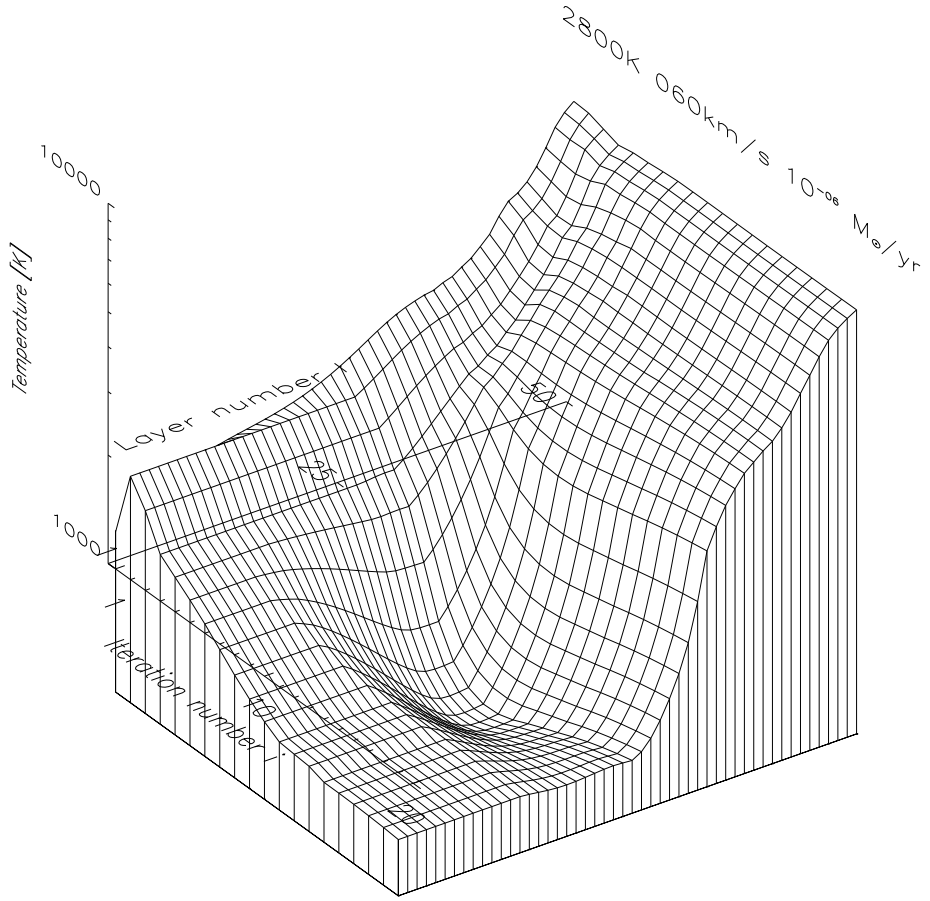

Figure 20: The temperature structure restores from a temperature inversion. The x-axis shows the iteration number i from 1 to 20, the y-axis the layer number l from 1 to 50, the z-axis shows the temperature logarithmically. In this case this is achieved by increasing the general `PHOENIX` temperature correction attenuation parameter `idmin`. The temperature fall consequently extends over more iterations and is more gradual so that the dip is smoother.

ation factor `idmin` (see the `PHOENIX` manual [Hau04]). By increasing `idmin` the temperature inversion develops more slowly. The final temperature structure is then approached in smaller steps and in a smoother way so that the dip does not get too deep. If the minimum is kept above 0 K, the structure has a chance to recover from the inversion. An example of a structure that was able to recover from the temperature inversion is shown in figure 20.

6.2 Sophistication of the temperature correction method

In figure 20 the constant temperature of the outer shells $l < 24$ has to decrease from 1900K after the second iteration $i = 2$ to 650K after the final iteration $i = 20$. This decrease is slow for the outermost layers $l < 12$ but too fast at first for the layers $12 < l < 24$. The structure does not start to recover from the temperature inversion until the temperature of the outermost layers $l < 12$ has approached the final outer temperature.

A much better way to handle the temperature inversions than the constant attenuation of the complete temperature correction with `idmin` would involve a modification to the temperature correction method. As stated in [Luc64] it is convenient to write the temperature correction ΔB in equation (53) as

$$\Delta B = \Delta B_1 + \Delta B_2 \tag{82}$$

with

$$\Delta B_1(r) = \frac{1}{\kappa_P}\{\kappa_J J - \kappa_P B + \dot{S}/(4\pi)\} \tag{83}$$

$$\Delta B_2(r) = -2(H(\tau = 0) - H_0(\tau = 0)) + \frac{1}{fqr^2}\int_r^R qr'^2 \chi_F (H(r') - H_0(r'))\mathrm{d}r' \tag{84}$$

The first term ΔB_1 is important for the outer layers but is always small in the deeper layers. The accurate correction in the deeper layers is obtained through the term ΔB_2. For the wind models the convergence of the inner layers is not problematic, but the region ΔB_1 is responsible for is. Especially the large corrections due to ΔB_1 are too large. Lucy [Luc64] has already suggested to under-correct the first term if the correction is large according to

$$\Delta B = \begin{cases} \Delta B_1 + \Delta B_2 & \text{if} \quad \Delta B/B < 0.1 \\ 0.8 \cdot \Delta B_1 + \Delta B_2 & \text{if} \quad \Delta B/B > 0.1 \end{cases} \tag{85}$$

The values of 0.1 and 0.8 might need to be revised for general purposes, or even become input parameters for single models to be tuned. Using this kind of attenuation of the temperature correction right at the place r where the correction would become too large could solve or at least improve the situation concerning the temperature inversions.

6.3 Adapted radial sampling

Apart from the fact that the temperature is nearly constant in the outer layers, as shown for a typical model in figure 19 to be over 30 of 35 wind layers, is a problem for the interpolation of the source function (see section

6.1) it suggests that the contribution of the outer shells to the final model spectrum is not very useful.

The cosh sampling function defined by equation (59) used in the wind model more finely samples the inner regions of the wind where the contribution is expected to be more important. The sampling depends on the parameter C as shown in figure 12. The improved C refinement introduced in section 4.5 has been implemented for better model convergence, but apparently the final sampling is still not optimal. It would be principally better to adapt the radial sampling to the wind velocity structure that is to be sampled.

6.3.1 Determination of an optimal sampling function

The basic idea for the adapted radial sampling is to adapt the number of layers to the importance of that specific region in proportion to that of other regions. Then many layers are reserved for regions where the wind is important and only a few layers in regions where the contribution to the spectrum is either very small or not different from the contribution of other layers.

At first, a criterium has to be defined in order to estimate the relative importance $\iota(r)$ of a specific shell with radius r. It is impossible to foretell the exact contribution a specific shell has to the spectrum, so the importance definition can only contain subjective criteria. As no absolute relations are needed it is sufficient to specify the proportionality of the importance to the different quantities. The following quantities are chosen to make up ι:

$v(r)$: The wind velocity is what makes the wind shells special when added to the hydrostatic region. The addition of a low velocity shell to the hydrostatic spectrum is not as interesting as a high velocity shell.

$\frac{\mathrm{d}v(r)}{\mathrm{d}r}$: The different velocities of different shells distinguishes them from each other. Where the gradient is large, many layers are needed to sample the differences.

$\rho(r)$: When the density of a shell is extremely low, no significant contribution of this shell is to be expected, whereas dense shells have a large impact on the radiation field. So many layers are needed for dense region and only a few for the thin regions.

In conclusion the relative importance of a shell with radius r is

$$\iota(r) \propto v(r) \cdot \frac{\mathrm{d}v(r)}{\mathrm{d}r} \cdot \rho(r) \tag{86}$$

In figure 21 the curve of $\iota(r)$ is plotted together with the three functions ι is constructed from for a β-law with the standard value $\beta = 3$.

Until now shells have been considered with a radial distance r. Now r is discretised to layers $r = r(l)$ with $l = 1, \ldots, l_*$. $\iota(r)$ can be expressed as a

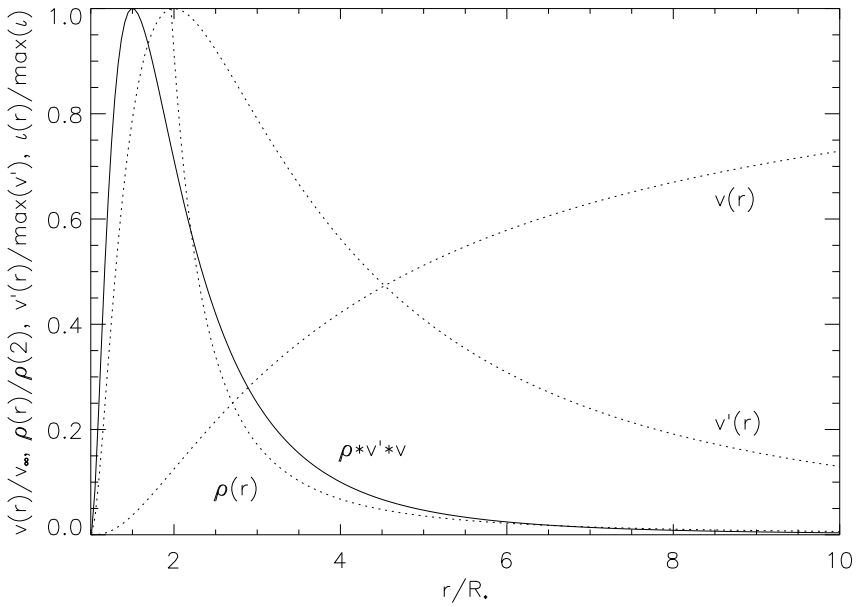

Figure 21: The importance of a shell of the hydrodynamic part of the atmosphere as defined by Eq. (86) normalised to a maximum of unity is the solid curve. The three functions comprised in ι are the dotted lines. The velocity is given by a β-law with the standard value $\beta = 3$. The radius is given in units of R_*. The shells very close to the star are not important because they are almost static $v \approx 0$ and do not change much $v' \approx 0$. The shells very far from the star are not very important because they become similar $v' \approx 0$ and thin $\rho \approx 0$.

function of the layer number l

$$\iota(l) = \iota(r(l)) \propto v(l) \cdot \frac{\mathrm{d}v(l)}{\mathrm{d}l} \cdot \rho(l) \tag{87}$$

which represents the importance of layer l and where $v(l) = v(r(l))$, $\frac{\mathrm{d}v(l)}{\mathrm{d}l} = \frac{\mathrm{d}v(r(l))}{\mathrm{d}r} \cdot \frac{\mathrm{d}r(l)}{\mathrm{d}l}$ and $\rho(l) = \rho(r(l))$.

The importance of the layers should be inverse proportional to the distance between the layers which is itself proportional to the sampling rate s, so that

$$s(l) \equiv \left(\frac{\mathrm{d}r(l)}{\mathrm{d}l}\right)^{-1} \propto \iota(l) \tag{88}$$

Using the continuity equation (1) this can be written as

$$\left(\frac{\mathrm{d}r(l)}{\mathrm{d}l}\right)^{2} \propto \frac{r^2}{\frac{\mathrm{d}v(l)}{\mathrm{d}r}} \tag{89}$$

This differential equation determines the adapted radial sampling function.

6.3.2 The exact solution for a β-law with $\beta = 3$

When $v(r)$ is a β-law with $\beta = 3$ Eq. (89) simplifies to

$$\frac{\mathrm{d}r(l)}{\mathrm{d}l} \propto \pm \frac{r^3(l)}{r(l) - R_*} \tag{90}$$

which can be solved analytically. This is an ordinary first order differential equation of the form

$$y' = f(y, t) \tag{91}$$

The solution $y(t)$ is determined by one initial value, e.g. $y(t_0) = y_0$. But the radial sampling function has two boundary values $r(1) = R_{\max}$ and $r(l_*) = R_{\min}$. Therefore, equation (90) must be written as

$$r'(l) = c \cdot \frac{r^3(l)}{r(l) - R_*} \tag{92}$$

in which the constant c is determined by the other boundary value. The solution of Eq. (92) is the (analytically) *adapted radial sampling function*

$$r_{\mathrm{a}}(l) \equiv -R_{\max}^2 \frac{(1+f)}{g} \tag{93}$$

in which the first boundary condition $r(l = 1) = R_{\max}$ is used and f and g are given by

$$f = \sqrt{2c(l-1) + \frac{(R_{\max} - 1)^2}{R_{\max}^2}} \tag{94}$$

$$g = 1 - 2R_{\max} + 2cR_{\max}^2(l-1) \tag{95}$$

With the second boundary condition $r(l = l_*) = R_{\min}$ the expression for c is found

$$c = \frac{1 - 2R_{\min} - \frac{R_{\min}^2}{R_{\max}^2} + \frac{2R_{\min}^2}{R_{\max}}}{2R_{\min}^2(l_* - 1)} \tag{96}$$

The three plots in figure 22 show the adapted radial sampling function of Eq. (93) in comparison with the usual cosh-function with a slope factor $C = 6.0$ used in the wind model for different values of $R_{\max}$. In figure 23 a plot of the radial importance distribution is shown, the adapted radial sampling function and the resulting layer importance distribution.

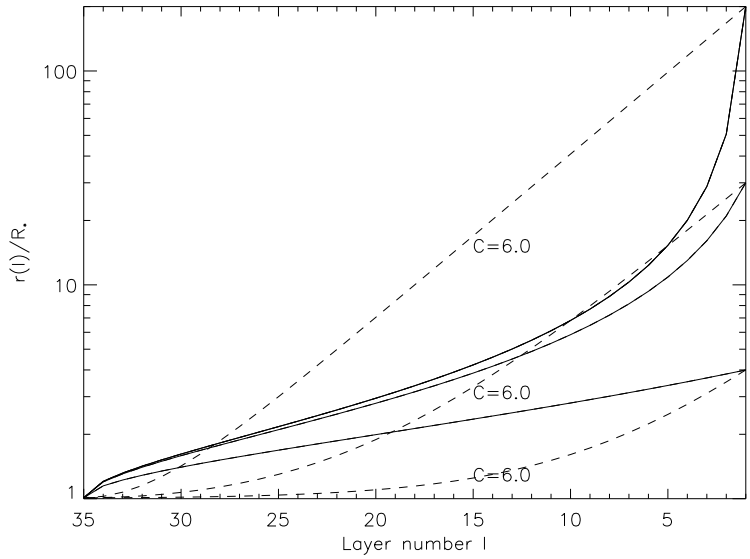

Figure 22: For three different values of $R_{\max} = 200$, 30 and $4R_\odot$ the adapted radial sampling curves are shown (solid lines) in comparison with the cosh curve (dashed lines) that is currently implemented in the wind model (Eq. (59)). The differences are substantial for all three values of $R_{\max}$. Both the extreme inner and the outer layers are sampled more coarsely with the adapted radial grid than with the cosh grid, which reflects the adaption to the importance distribution (see figure 21).

6.3.3 Estimating sampling qualities

When the adapted radial sampling function of Eq. (93) is used the importance of layer l is by design (Eq. (88)) equal to the radial sampling rate $s(l)$. This means that the radial distribution of the layers $r(l)$ is optimal, according to the chosen form of ι. The radial distribution of other radial sampling functions, like the cosh function of Eq. (59) used to construct the radial grid in the wind model, consequently are not optimal. The importance function gives an opportunity to test models for their radial sampling quality. For that purpose the quality function q is defined as square root of the product of the normalised importance and the normalised radial sampling rate

$$q(l) \equiv \sqrt{\frac{1}{a}\iota(l) \cdot \frac{1}{b}s(l)} \tag{97}$$

The coefficients

$$a = \sum_{l=1}^{l_*} \iota_{\rm a}(l) \tag{98}$$

$$b = \sum_{l=1}^{l_*} s_{\rm a}(l) \tag{99}$$

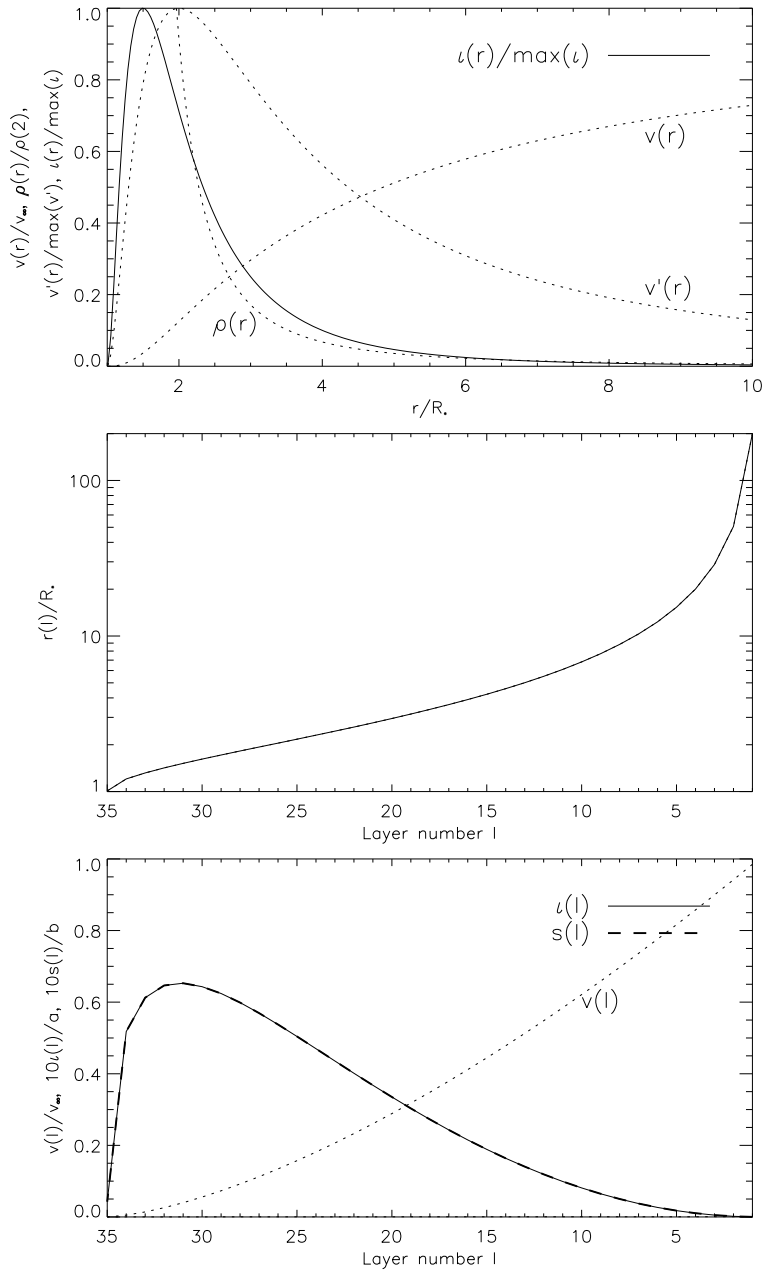

Figure 23: The adapted radial sampling function (center graph) transposes the radial structure information $v(r)$, $\mathrm{d}v(r)/\mathrm{d}r$ and $\rho(r)$ (top graph) in such a way, that the sampling rate $s(l)$ is large (the distance between the layers is small) where the importance $\iota(l)$ of a layer is large (bottom graph).

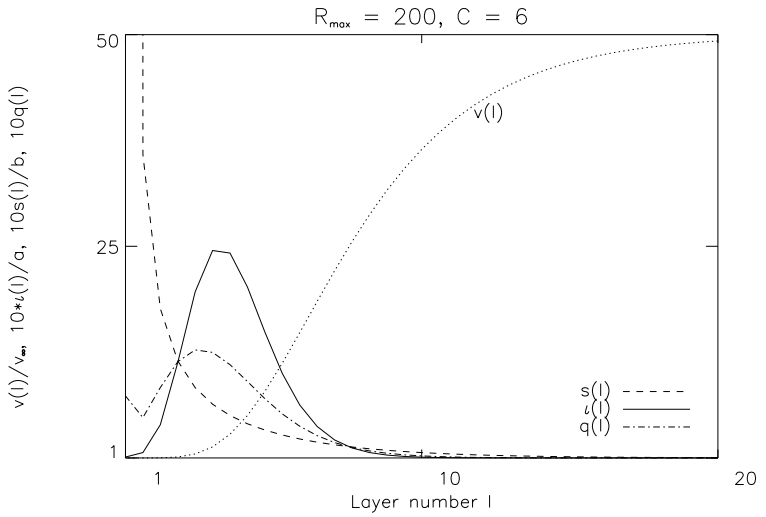

Figure 24: The importance ι, sampling rate s and the quality function q for the radial cosh grid used in the wind model (Eq. (59)). The importance function is more localised than when the adapted radial sampling function (Eq. (93)) is used (for comparison see the bottom graph of figure 23).

normalise the integrated importance and the radial sampling rate to unity for the adapted sampling function. The square root maintains the normalisation.

As for the adapted radial sampling function $q_{\rm a}(l) = \iota_{\rm a}(l) = s_{\rm a}(l)$, the quality function is spread out over all layers (see the bottom graph of figure 23). For other sampling functions $q(l)$ is more localised. In case of the cosh function, q is typically spread out over about 15 layers of 35. An example for $R_{\rm max} = 200 R_\odot$ and $C = 6$ is shown in figure 24.

$q(l)$ represents the contribution of layer l to the total quality of the radial sampling Q

$$Q = \sum_{1}^{l_*} q(l) \tag{100}$$

This *quality index* Q can be used to compare the quality of various sampling functions. Because of the normalisation coefficients a and b the quality index for the adapted sampling function for $\beta = 3$ (Eq. (93)) equals unity $Q_{\rm a} = 1$. This reflects the fact that the adapted sampling is assumed to supply the "optimal" radial sampling. The square root in equation (97) ensures that the contribution to Q of layers for which $\iota \cdot s$ is small are not underrepresented.

The Q values for the cosh sampling function (Eq. (59)) for various C and $R_{\rm max}$ are shown in table 2. Some corresponding quality curves are shown in the appendix. The low values for $R_{\rm max} = 200 R_\odot$ are caused by the fact that the cosh function oversamples the outer region (see figure 22), which is

C	Q		
	$R_{\max} = 200$	$R_{\max} = 20$	$R_{\max} = 2$
1	0.056	0.260	0.689
2	0.064	0.296	0.674
3	0.080	0.355	0.650
4	0.106	0.432	0.619
5	0.147	0.513	0.586
6	0.203	0.583	0.556
7	0.270	0.630	0.528
8	0.337	0.652	0.502
9	0.395	0.654	0.480
10	0.438	0.641	0.461
11	0.465	0.620	0.447
12	0.477	0.599	0.435

Table 2: The quality index Q for the cosh sampling function as implemented in the wind model for various C and $R_{\max}$. Q gives an upper boundary for the wind sampling quality. For the adapted radial sampling function $Q = 1$. The maximum values for each $R_{\max}$ occur at different values for C. Graphs of quality curves corresponding to a number of the Q values in this table can be found in the appendix (figure 26-28).

very large in this case. The best value of C is the highest of the range listed in the table, because for higher values the innermost region is sampled even better.

This shows the weakness of the quality testing method: a poor sampling of important layers can be compensated by an oversampling of unimportant regions. Another weakness appears if a sampling function would situate all layers in that region where $\iota(r)$ is high ($1.25 \lesssim r \lesssim 2/, R_*$ for the case of a $\beta = 3$ velocity field, see figure 23). Then both $\iota(l)$ and $s(l)$ are large in all layers, resulting in a high Q (even larger than 1), although only a very small region of the wind is sampled. However, these weaknesses both do not largely affect Q for the adaptive radial sampling function. Q for the cosh function is affected by the first weakness, which causes the value to be too large. It is not affected by the second problem, because the region with large $\iota(r)$ is rather undersampled than oversampled.

In conclusion, the Q values listed in table 2 are upper boundaries. Therefore, the adapted radial grid would improve the quality of the wind modelling considerably.

6.3.4 A numerical method for arbitrary velocity fields

The differential equation that determines the adapted radial sampling function (Eq. (89)) can generally not be solved for arbitrary values of β or non-β-law velocity fields. Although β has not been varied for calculations performed in the scope of this work, it is an important wind modelling pa-

rameter. Therefore, a more general version of the adapted radial sampling method is needed.

Instead of the assumption of equation (88), for the numerical solution it is assumed that the importance integrated over a layer should be equal for all layers $1 \leq l \leq l_*$

$$\int_{r(l)}^{r(l+1)} \iota(r)\,\mathrm{d}r = \frac{1}{l_*-1}\int_{r(l_*)}^{r(1)} \iota(r)\,\mathrm{d}r = \frac{1}{l_*-1}\int_{R_{\min}}^{R_{\max}} v(r)\frac{\mathrm{d}v(r)}{\mathrm{d}r}\rho(r)\,\mathrm{d}r \quad (101)$$

The factor $1/(l_*-1)$ represents the l_*-1 intervals the importance is divided over. This defines the *numerically adapted radial grid* $r_\mathrm{n}(l)$.

When equation (101) is evaluated the integral is replaced by a summation and

$$\frac{\mathrm{d}v(r)}{\mathrm{d}r} = \frac{v(r_{i+1}) - v(r_{i-1})}{r_{i+1} - r_{i-1}} \quad (102)$$

But the largest part of the contribution to the integrated importance is obtained within the first few stellar radii (see figure 21), whereas the last radius of the outermost grid point is a few hundred stellar radii. Consequently, very small radial steps are needed to obtain a reasonably accurate numerically adapted radial grid $r_\mathrm{n}(l)$.

The numerically adapted grid for a β-law with $\beta = 3$ is computed (with 7000 radial points in the interval $R_{\min} - R_{\max}$) for comparison with the analytic solution of section 6.3.2. The obtained sampling curve is virtually equal to analytic solution r_a, shown in figure 23. But when the importance $\iota(l)$ and the sampling rate $s(l)$ are calculated from r_n the inaccuracy is noticeable, see figure 25.

6.3.5 The limitations and the benefits of adapted sampling

The analytical and the numerical method presented here are based on an importance relation that specifies the relative importance of a shell with radius r. Such an importance consideration is only very approximative and based on a subjective choice of contributing quantities. Therefore, the importance should be carefully chosen and possibly the results for multiple importance relation must be compared.

A better definition of the importance relation could comprise replacing the ρ of equation (86) by the optical depth τ_std. As τ_std is not known a priori, this can not be used for an initial radial grid. A model could be started with an initial grid based on ρ for the importance. In subsequent iterations this initial grid can then be refined using the optical depth for the importance definition.

As in practice the flexibility of the model for importance definitions and velocity fields is required, the analytic method is not generally useful.

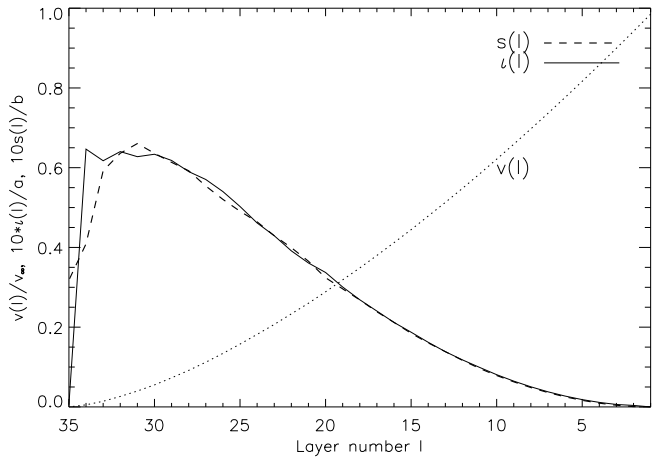

Figure 25: The importance ι and the sampling rate s for a $\beta = 3$ velocity field as obtained by the numerical method of section 6.3.4. The result is the same as with the analytic solution of section 6.3.2 except that it is less accurate (see figure 23 for comparison).

The numerical method is not very accurate but usable, because the exact location of a single layer is not important. Some scattering around the actual value can be tolerated. But another numerical method, which is more accurate than the method described in section 6.3.4, is to numerically solve the differential equation (89). For example a Runge-Kutta method could be used.

The original problem the adapted sampling has been proposed for is the constant temperature in the outer shells of the wind models. Due to these outer shells, `taulin` needs to be increased to assure a linear interpolation of the (rather) constant source function. With the adapted radial sampling the temperature (and the source function) will not be constant over numerous layers anymore. Thus the parabolic interpolation can be used for larger steps in the optical depth along a characteristic ray (`taulin` can be decreased). This in turn prevents the inner wind region from temperature inversions (section 6.1).

6.4 Outlook

In the foregoing discussion two suggestions for improvement of the wind model have been described. The first is the sophistication of the temperature correction method (section 6.2). This should improve the ability to construct converging models for winds with high mass loss rates or low terminal velocities (which both lead to increasing wind densities). The implementation comprises a determination of good values for the two constants in equation (85).

The second one is to implement the adapted radial grid (section 6.3). This improves the convergence because the more precise parabolic interpolation can be used for the ALI method instead of the linear. In addition, the adapted radial grid improves the accuracy of the wind spectrum, because a larger diversity of wind shells is being sampled. The coarser sampling of the innermost wind shells leads to larger steps in the optical depth for this region. Therefore, the temperature correction sophistication is a prerequisite for this new grid. Probably, the number of wind layers has to be increased and thus the total number of model layers. For the implementation of the adapted radial grid the effect of alternative definitions of the importance function needs to be analysed. For the analysis of the actual contribution of a layer to the spectrum depth (layer) dependent spectra could be used.

All calculations performed in the scope of this work have been made with the assumption of LTE, which is a good approximation only when the level populations are dominated by collisions. But in the wind layers the densities are very small so that collisions become very rare. Consequently, LTE is expected to be a very poor assumption for the wind region. Non-LTE calculations are needed for accurate cool-wind modelling.

With the increased accuracy of the adapted sampling and NLTE, the effects of more complicated semi-empirical velocity fields like the ζ Aurigae field from [BKR$^+$96] (figure 8) can be examined or even refined to better fit the observations.

A Quality curves for the cosh sampling function

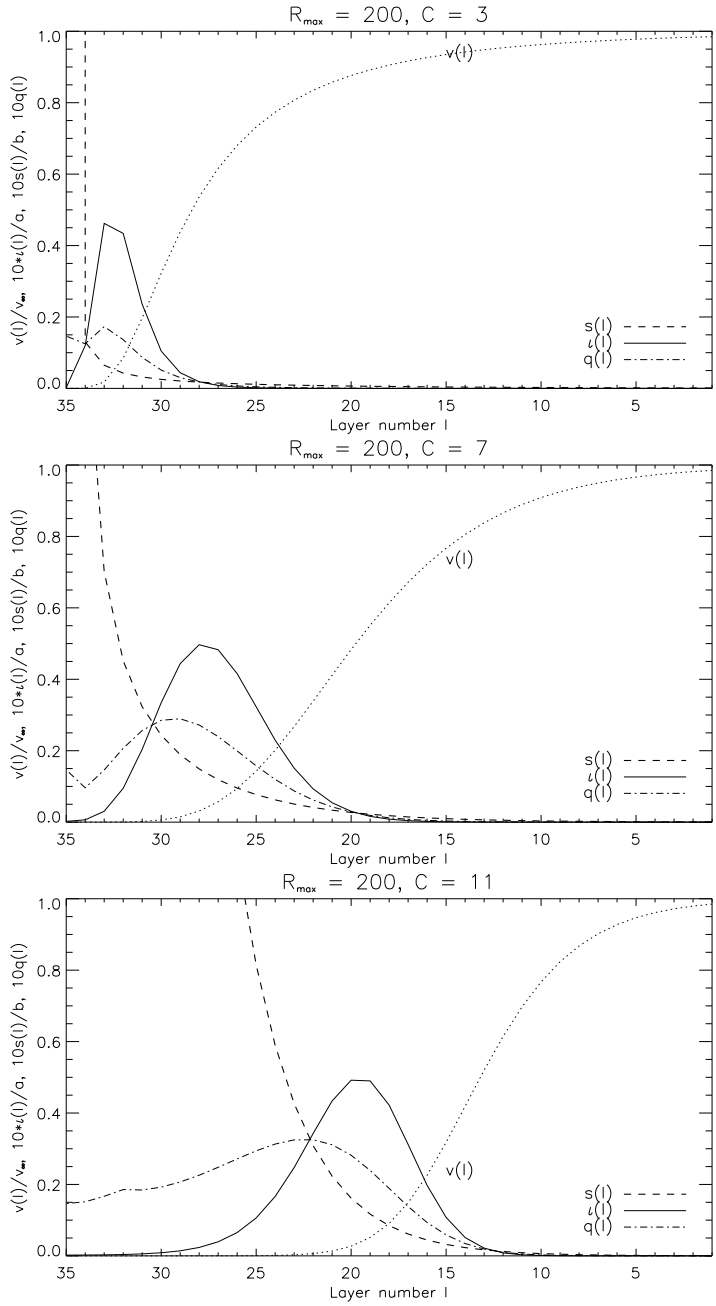

Figure 26: Curves for the importance distribution ι, the sampling rate s and the resulting quality distribution q for the cosh sampling function with $C = 3, 7, 11$ and $R_{\max} = 200R_{\odot}$. The area under the dashdotted q-curve is an estimation of the sampling quality.

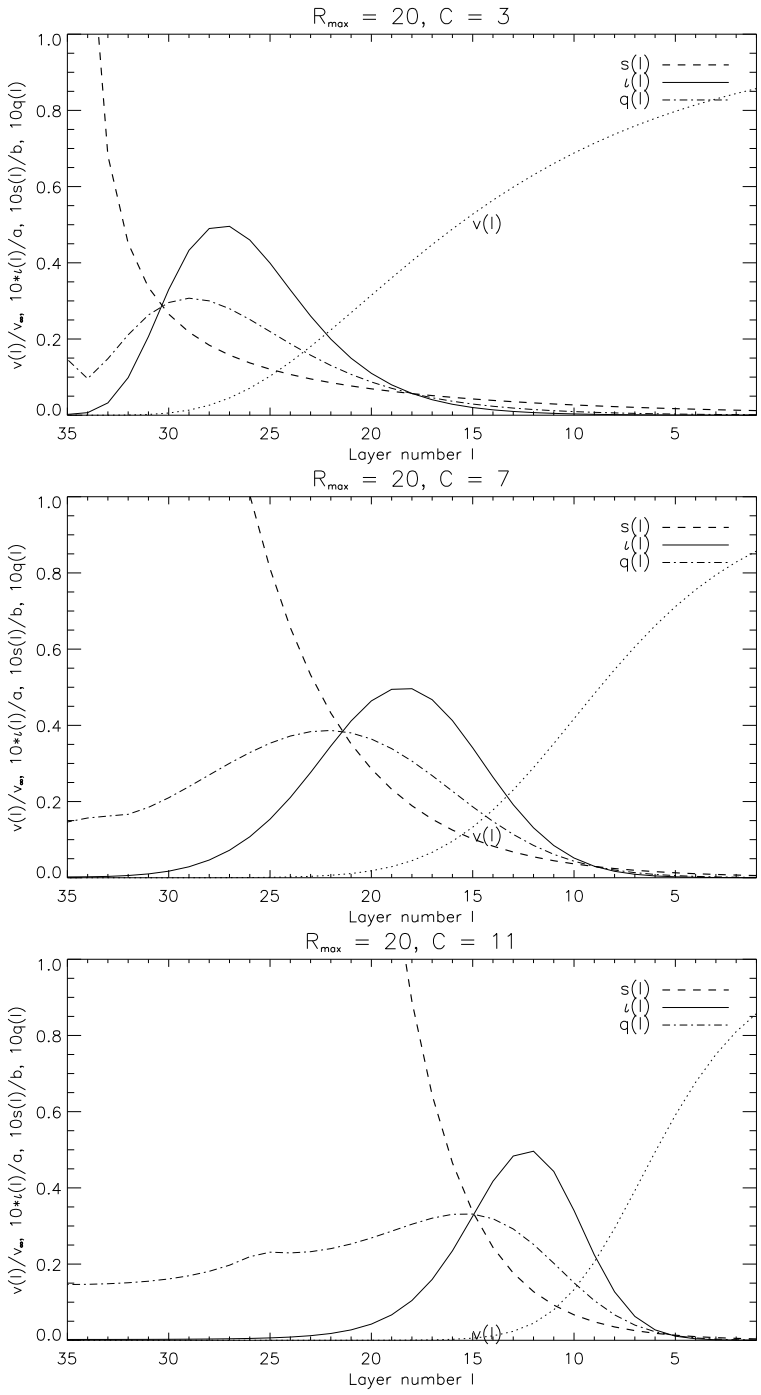

Figure 27: Like figure 26, but with $R_{\max} = 20R_{\odot}$.

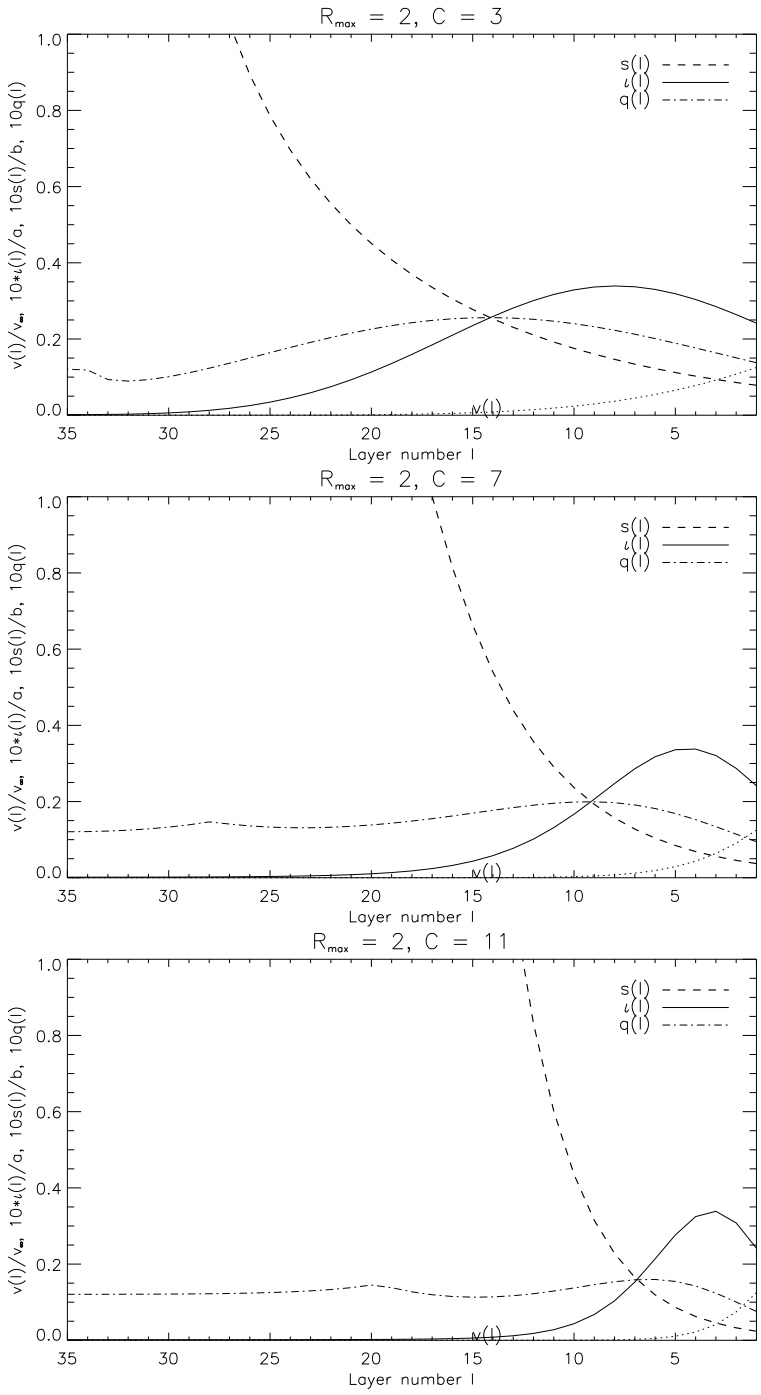

Figure 28: Like figure 26, but with $R_{\max} = 20R_{\odot}$.

References

[Auf00] Aufdenberg, J. P.: Line-blanketed spherically extended model atmospheres of hot luminous stars with and without winds. In: *Ph.D. Thesis* (2000), August

[Baa92] Baade, R.: Line formation in multi-dimensional atmospheres with arbitary velocity fields. In: Jeffery, C. S. (Hrsg.) ; Griffin, R. E. M. (Hrsg.): *Stellar Chromospheres, Coronae and Winds*, 1992, S. 49–+

[BBB+01] Brown, A. ; Bennett, P. D. ; Baade, R. ; Kirsch, T. ; Reimers, D. ; Hatzes, A. P. ; Kürster, M.: Ultraviolet Eclipse Observations and Fundamental Parameters of the Binary HR 2554 (G6 II+A1 V). In: *AJ* 122 (2001), Juli, S. 392–401. http://dx.doi.org/10.1086/321125. – DOI 10.1086/321125

[Ben05] Bennett, P.: *Empirical Modelling of Cool Star Chromospheres and Winds*. Seminar at the Hamburger Sternwarte, November 2005

[BH97] Bennett, P. D. ; Harper, G. M.: Semi-Empirical Wind Models for lambda Velorum (K4 Ib-II). In: Clarke, D. A. (Hrsg.) ; West, M. J. (Hrsg.): *ASP Conf. Ser. 123: Computational Astrophysics; 12th Kingston Meeting on Theoretical Astrophysics*, 1997, S. 87–+

[BKR+96] Baade, R. ; Kirsch, T. ; Reimers, D. ; Toussaint, F. ; Bennett, P. D. ; Brown, A. ; Harper, G. M.: The Wind Outflow of zeta Aurigae: A Model Revision Using Hubble Space Telescope Spectra. In: *ApJ* 466 (1996), August, S. 979–+. http://dx.doi.org/10.1086/177569. – DOI 10.1086/177569

[BM86] Brosius, J. W. ; Mullan, D. J.: Models of transition regions in hybrid stars. In: *ApJ* 301 (1986), Februar, S. 650–663. http://dx.doi.org/10.1086/163931. – DOI 10.1086/163931

[Bra70] Brandt, J.C.: *Introduction to the Solar Wind*. Freeman (San Fancisco), 1970

[CAK75] Castor, J. I. ; Abbott, D. C. ; Klein, R. I.: Radiation-driven winds in Of stars. In: *ApJ* 195 (1975), Januar, S. 157–174

[Cha81] Chapman, R. D.: The 1979-1980 eclipse of Zeta Aurigae. I - The circumstellar envelope. In: *ApJ* 248 (1981), September, S. 1043–1052. http://dx.doi.org/10.1086/159233. – DOI 10.1086/159233. – Shock cone from ultrasonic movement of the secondary in ζ Aurigae systems

[CRH+99] Carpenter, K. G. ; Robinson, R. D. ; Harper, G. M. ; Bennett, P. D. ; Brown, A. ; Mullan, D. J.: GHRS Observations of Cool, Low-Gravity Stars. V. The Outer Atmosphere and Wind of the Nearby K Supergiant lambda Velorum. In: *ApJ* 521 (1999), August, S. 382–406. http://dx.doi.org/10.1086/307520. – DOI 10.1086/307520

[Deu56] Deutsch, A. J.: The Circumstellar Envelope of Alpha Herculis. In: *ApJ* 123 (1956), März, S. 210–+

[DSL92] Dupree, A. K. ; Sasselov, D. D. ; Lester, J. B.: Discovery of a fast wind from a field population II giant star. In: *AJL* 387 (1992), März, S. L85–L88. http://dx.doi.org/10.1086/186311. – DOI 10.1086/186311. – rapid wind accelleration to 100km/s

[HA84] Hartmann, L. ; Avrett, E. H.: On the extended chromosphere of Alpha Orionis. In: *ApJ* 284 (1984), September, S. 238–249. http://dx.doi.org/10.1086/162402. – DOI 10.1086/162402. – determination of the α Ori velocity structure

[Har96] Harper, G.: Mass loss and winds from cool giants. In: Pallavicini, R. (Hrsg.) ; Dupree, A. K. (Hrsg.): *ASP Conf. Ser. 109: Cool Stars, Stellar Systems, and the Sun*, 1996, S. 481–+

[Hau92] Hauschildt, P. H.: A fast operator perturbation method for the solution of the special relativistic equation of radiative transfer in spherical symmetry. In: *JQSRT* 47 (1992), S. 433

[Hau04] Hauschildt, P.H.: PHOENIX *Version 13 Manual*. http://-www.hs.uni-hamburg.de/EN/For/ThA/phoenix/documents-/Manual/Manual.pdf, August 2004

[HB98] Hauschildt, P. H. ; Baron, E.: Numerical Solution of the Expanding Stellar Atmosphere Problem. In: *ArXiv Astrophysics e-prints* (1998), August

[HB04] Hauschildt, P. H. ; Baron, E.: Improved discretization of the wavelength derivative term in CMF operator splitting numerical radiative transfer. In: *A&A* 417 (2004), April, S. 317–324. http://dx.doi.org/10.1051/0004-6361:20034473. – DOI 10.1051/0004–6361:20034473

[HBB+05] Harper, G. M. ; Brown, A. ; Bennett, P. D. ; Baade, R. ; Walder, R. ; Hummel, C. A.: VLA Observations of

ζ Aurigae: Confirmation of the Slow Acceleration Wind Density Structure. In: *AJ* 129 (2005), Februar, S. 1018–1034. http://dx.doi.org/10.1086/426908. – DOI 10.1086/426908

[HBBA03] Hauschildt, P. H. ; Barman, T. S. ; Baron, E. ; Allard, F.: Temperature Correction Methods. In: Hubeny, I. (Hrsg.) ; Mihalas, D. (Hrsg.) ; Werner, K. (Hrsg.): *ASP Conf. Ser. 288: Stellar Atmosphere Modeling*, 2003, S. 227–+

[HDJB85] Hartmann, L. ; Dupree, A. K. ; Jordan, C. ; Brown, A.: On the outer atmospheres of hybrid stars. In: *ApJ* 296 (1985), September, S. 576–592. http://dx.doi.org/10.1086/163476. – DOI 10.1086/163476

[HDR81] Hartmann, L. ; Dupree, A. K. ; Raymond, J. C.: On the relationship between coronae and mass loss in late-type stars. In: *ApJ* 246 (1981), Mai, S. 193–202. http://dx.doi.org/10.1086/158911. – DOI 10.1086/158911. – α TrA velocity structure

[HM85] Holzer, T. E. ; MacGregor, K. B.: Mass loss mechanisms for cool, low-gravity stars. In: Morris, M. (Hrsg.) ; Zuckerman, B. (Hrsg.): *ASSL Vol. 117: Mass Loss from Red Giants*, 1985, S. 229–255

[HW82] Huang, R. Q. ; Weigert, A.: Shock fronts in wide binary systems. In: *A&A* 112 (1982), August, S. 281–286. – Interaction of two stellar winds in binary systems

[JJ91] Judge, P. G. ; Jordan, C.: Fe II emission lines. I - Chromospheric spectra of red giants. In: *AJS* 77 (1991), September, S. 75–95. http://dx.doi.org/10.1086/191599. – DOI 10.1086/191599

[KB94] Kirsch, T. ; Baade, R.: The expanding envelope of zeta Aurigae. In: *A&A* 291 (1994), November, S. 535–545

[KPPA89] Kudritzki, R. P. ; Pauldrach, A. ; Puls, J. ; Abbott, D. C.: Radiation-driven winds of hot stars. VI - Analytical solutions for wind models including the finite cone angle effect. In: *A&A* 219 (1989), Juli, S. 205–218

[Lam97] Lamers, H. J. G. L. M.: The Theory of Line Driven Stellar Winds. In: *LNP Vol. 497: Stellar Atmospheres: Theory and Observations* 497 (1997), S. 159–+

[LB91] Lafon, J.-P. J. ; Berruyer, N.: Mass loss mechanisms in evolved stars. In: *A&AR* 2 (1991), April, S. 249–289

[LC99] Lamers, Henny J. ; Cassinelli, Joseph P.: *Introduction to stellar winds*. Freeman (San Fancisco), 1999

[LH79] Linsky, J. L. ; Haisch, B. M.: Outer atmospheres of cool stars. I - The sharp division into solar-type and non-solar-type stars. In: *AJL* 229 (1979), April, S. L27–L32. http://dx.doi.org/10.1086/182924. – DOI 10.1086/182924

[Luc64] Lucy, L. B.: A Temperature-Correction Procedure. In: *SAO Special Report* 167 (1964), Dezember, S. 93–+

[Mih80] Mihalas, D.: Solution of the comoving-frame equation of transfer in spherically symmetric flows. VI - Relativistic flows. In: *ApJ* 237 (1980), April, S. 574–589. http://dx.doi.org/10.1086/157902. – DOI 10.1086/157902

[MW84] Mihalas, D. ; Weibel Mihalas, B.: *Foundations of radiation hydrodynamics*. New York: Oxford University Press, 1984, 1984

[OK87] Olson, G. L. ; Kunasz, P. B.: Short characteristic solution of the non-LTE line transfer problem by operator perturbation. I. - The one-dimensional planar slab. In: *JQSRT* 38 (1987), S. 325

[Par58] Parker, E. N.: Dynamics of the Interplanetary Gas and Magnetic Fields. In: *ApJ* 128 (1958), November, S. 664–+

[Par71] Parker, E. N.: Recent Developments in Theory of Solar Wind. In: *Reviews of Geophysics and Space Physics* 9 (1971), S. 825–835

[RL79] Rybicki, G. B. ; Lightman, A. P.: *Radiative processes in astrophysics*. New York, Wiley-Interscience, 1979. 393 p., 1979

[Rut95] Rutten, R.: *Radiative transfer in stellar atmospheres*. 1995

[Vog91] Vogel, M.: Empirical velocity laws for cool giants. I - The symbiotic binary EG Andromedae. In: *A&A* 249 (1991), September, S. 173–180

[Wik06] Wikipedia: *Aurora*. http://en.wikipedia.org/wiki/Aurora, May 2006

Acknowledgements

First I am delighted to thank Prof. Peter H. Hauschildt for providing me with the very interesting topic, exactly the kind of topic I wished to have, and helping me with the successful execution of this work.

I thank Prof. J. Schmitt for reading my work as second referee.

Thanks to Dr. Robert Baade, the ultimate specialist in the field of cool winds, for supplying me with exactly those papers I needed at the time I needed them most. Those papers and the references therein have been the basis of this work.

Throughout this work Andy uncountable times helped me to make the computers act as I hoped them to work. I thank him for this great help. His tips always worked, all of the problems he just solved immediately.

And a very big THANKS to Christine and Knop. Both my roommates have helped me in so many respects. Funny enough, their tips always were mutual exclusive, I could use them both! I thank Christine, who time by time again convinced me, that I should start (and continue) writing instead of mourning about unsatisfactory unfinished results. Thanks also for your tips to improve my style of writing. Thanks to Knop, who was a great help to me when I started with the topic helping me to understand what I was going to do, either the physical and the technical side of the moon. I also want to thank him for the endless patience in trying to understand my curious ideas and asking questions that made me clear up my mind. Also thanks for reading my work so thoroughly.

Furthermore, I want to thank Oom Piet and Tante Cora for continuously encouraging me and their unbelievable support to finish my study!

Finally, I thank my lovely wife Silke for always being at my side and for her aid in doing my work by her care for the children and for everything else.

Erklaerung

Hiermit versichere ich, Daniël R. van Rossum, die vorliegende Arbeit selbstaendig verfasst und nur unter Zuhilfenahme der angegebenen Quellen und Hilfsmittel angefertigt zu haben. Desweiteren erklaere ich mich mit dem Verleih und der Veroeffentlichung dieser Arbeit einverstanden.

Hamburg, den 31.05.2006

Unterschrift